Reverse Water Gas Shift Reaction over High Surface Area γ-Al_2O_3 Supported Mo_2C Nanoparticles Synthesized by Reverse Microemulsion Method

by

Guanjie Sun

A thesis

presented to the University of Waterloo

in fulfilment of the

thesis requirement for the degree of

Master of Applied Science

in

Chemical Engineering

Waterloo, Ontario, Canada, 2019

AUTHOR'S DECLARATION

I hereby declare that I am the sole author of this thesis. This is a true copy of the thesis, including any required final revisions, as accepted by my examiners.

I understand that my thesis may be made electronically available to the public.

Abstract

Increasing concentrations of greenhouse gases (GHG), especially carbon dioxide (CO_2), in the atmosphere are forecasted to result in adverse environmental impacts. One attractive approach for mitigation of CO_2 emissions is utilizing this gas for the production of renewable synthetic fuels and chemicals. In particular, the reverse water gas shift (RWGS) reaction converts CO_2 to CO, which can further be used to generate valuable chemicals. In this study, MoOx and Mo_2C nanoparticles were synthesized by the reverse microemulsion method and analyzed their performance as RWGS catalysts. The catalyst composition, morphology and crystalline structure were investigated by inductively coupled plasma – optical emission spectrometry (ICP-OES), Brunauer-Emmett-Teller (BET) method, X-ray diffraction (XRD), temperature programmed reduction (TPR), transmission electron microscope (TEM) and scanning electron microscope (SEM). The impact of using different preparation method (e.g. reverse microemulsion versus impregnation method) on the catalytic activity, selectivity, and stability were determined using a fixed bed reactor experimental setup. The thermal decomposition processes of the spent catalysts were investigated using thermogravimetric analysis-Fourier Transform Infrared spectroscopy (TGA/FTIR). Overall findings have indicated that Mo_2C nanoparticles prepared by the reverse microemulsion method showed higher conversion, 100% selectivity to CO, and significantly more stable performance over extended times on stream than the commercial catalyst, $Cu/ZnO/Al_2O_3$ for the RWGS reaction.

Key words: RWGS reaction, $Mo_2C/\gamma\text{-}Al_2O_3$, $MoOx/\gamma\text{-}Al_2O_3$; Reverse Microemulsion method

Acknowledgements

I would like to thank my supervisors, Professor David Simakov and Professor Luis Ricardez-Sandoval for their patience, insight, support and guidance throughout my master's program.

I would also like to thank my committee members: Professor Eric Croiset, Professor Aiping Yu for their constructive comments and suggestions on my research project. Special thanks to my group members Yichen Zhuang, Muhammad Waqas Iqbal, Robert Currie, Sogol Mottaghi-Tabar and Yue Yu. Without them this project wouldn't have been possible.

Lastly, thank you to my family and friends for their encouragement and support through my project.

I would also like to acknowledge the support of the Waterloo Institute of Sustainable Energy (WISE), the Ontario Centers of Excellence (OCE), the Canada Foundation for Innovation (CFI), the Natural Science and Engineering Research Council (NSERC) of Canada and State Key Laboratory of Engine Reliability.

Table of Contents

Table of Figures

List of Tables

Nomenclature

λ	wavelength of the X-ray
n	any positive integer
d	plane spacing
θ	the grazing angle
p	the pressure at equilibrium
p_2	the saturated vapor pressure of the adsorbed gas
V_m	the volume of gas required to form a monolayer on the surface
V	the amount of adsorption
C	constant
N_A	Avogadro constant
s	adsorption cross-sectional area of the adsorbed species
V	molar volume of the adsorbed species
a	quality of the adsorbent material.
y_i	mole fraction (i stands for either CO_2, CO, or CH_4)
$F_{H2,f}$	feed molar flow rate of H_2
α	H_2:CO_2 ratio in the feed
$F_{CO2,f}$	feed molar flow rate of CO_2
X_{CO2}	CO_2 conversion
f_2	CO_2 conversion to CH_4
$F_{CO,out}$	outlet molar flow rate of CO
f_1	CO_2 conversion to CO
$F_{C,out}$	total outlet molar flow rate of carbon
$F_{t,out}$	total outlet molar flow rate
$F_{CH4,out}$	outlet molar flow rate of CH_4
Q_f	volumetric feed flow rate
S_{CO}	selectivity to CH_4
W_c	catalyst weight
ΔH_{298}°	reaction enthalpy

Abbreviations

CB	carbon balance
GHSV	gas hourly space velocity
GHG	greenhouse gas
RWGS	reverse water gas shift
RME	reverse microemulsion method
RME-WI	reverse microemulsion – wet impregnation method
ca	Citra (approximately)
wt.	weight percent

Chapter 1

Introduction

1.1 Problem Statement and Motivation

Based on current trends and policies, worldwide energy consumption is expected to increase 30% by 2040 by the International Energy Agency (IEA) [1]. Resulting CO_2 emissions associated with this increase pose a major problem to the global ecosystem. For the purpose of hindering the progression of climate change and ocean acidification, CO_2 capture, storage, sequestration and utilization technologies must play a prominent role in the upcoming decades [2]. Carbon capture and storage (CCS), also known as carbon capture and sequestration, is a technology of capturing carbon dioxide emissions usually produced from large contributor sources, for example, manufacturing industrial processes and the use of fossil fuels in power plants, transporting the CO_2 captured to a storage site, and depositing and securely storing the carbon dioxide emissions, generally underground in depleted oil and gas fields or deep saline aquifer formations. Carbon capture and utilization (CCU) is the process of capturing carbon dioxide waste emissions from large emitters and to be produced new products and economic opportunities. Both CCS and CCU approaches require carbon capture, whereas the last step is completely different. Most mature CO_2 capture techniques such as post, pre and oxy-combustion are energy intensive and thus, expensive, however novel emerging technologies like CLC may reduce the energy penalty.[3-8].

Long-term storage options for the captured carbon dioxide and the unknown long-term consequences of storing CO_2 underground pose several unique challenges and problems for carbon capture and storage. Alternatively, carbon capture and

utilization for further development of useful synthetic chemicals from waste CO_2 provides an attractive route for the reduction of CO_2 emissions [9]. Different chemical pathways are available for CO_2 conversion: thermocatalytic reduction, biological conversion, electrochemical and photocatalytic reductions are the current pathways to produce synthetic chemical and fuels from CO_2. Among these approaches, thermocatalytic conversion of carbon dioxide is of particular promising. If using CO_2 as a fuel source or building block to create sustainable, green fuels and chemicals, the potential benefits of reducing the dependence on non-renewable sources would be achieved. Additionally, if utilizing intermittent energy sources like hydro, wind and solar to make useful chemicals from CO_2, the energy could be stored in a chemical form using pre-existing infrastructure and deployed when it's needed. In addition, thermocatalytic conversion of CO_2 into valuable fuels and useful chemicals is of specific compelling since this route enables CO_2 recycling and introducing of sustainable energy into the manufacturing chain of chemical industry [10-12]. One prohibitive factor for the implementation of the large-scale biofuel generation is the expense for the development and maintenance of biomass growth systems [13]. Research in the photocatalytic and electrochemical CO_2 conversion has an important potential; however these approaches are restricted by the low CO_2 solubility in water and transport limitations at low temperatures [13-16].

Thermocatalytic reduction shows great promise as it combines heterogeneous catalysis with high temperatures resulting in more advantageous kinetics, higher product throughput and technical feasibility, considering its similarity to some existing well-established industrial processes [13]. In particular, the reverse water gas shift (RWGS) reaction, Eq. (1), has been considered a viable process for CO_2 utilization. Product CO provides feedstock to the Fischer-Tropsch process, Eq. (2), which is well

established and well characterized in current industry to produce chemicals and synthetic fuels from syngas ($CO+H_2$) [9, 17] or methanol synthesis, Eq. (3). This alternative gives high efficiency for conversion of CO_2 captured from different waste stream and the flexibility in types of product.

$$CO_2 + H_2 \rightleftarrows CO + H_2O \quad \Delta H^\circ_{298K} = +41.2\ kJ/mol \tag{1}$$

$$(2n+1)H_2 + nCO \rightarrow C_nH_{2n+2} + nH_2O \quad \Delta H^\circ_{298K} = -162.5 kJ/mol \tag{2}$$

$$CO + 2H_2 \rightleftarrows CH_3OH \quad \Delta H^\circ_{298K} = -90.84 kJ/mol \tag{3}$$

Similar thermocatalytic pathways are the Sabatier reaction, Eq. (4), and CO Methanation, Eq. (5) [18].

$$CO_2 + 4H_2 \rightleftarrows CH_4 + 2H_2O \quad \Delta H^\circ_{298K} = -164.9\ \text{kJ/mol} \tag{4}$$

$$CO_2 + 3H_2 \rightleftarrows CH_4 + H_2O \quad \Delta H^\circ_{298K} = -206.1\ \text{kJ/mol} \tag{5}$$

1.2 Project Objectives

The RWGS reaction is reversible and mildly endothermic. As a result, large CO_2 conversions would be achieved at high temperatures. However, thermally induced deactivation (e.g. sintering) of catalysts generally occurs at high temperatures, resulting from the loss of catalytic surface area and support area. In addition, increasing temperatures promote CH_4 production which is an undesirable byproduct for this reaction. The noble metals (Pd, Pt) supported on metal oxide (TiO_2,Al_2O_3,CeO_2), Cu-based catalysts, Iron-based catalysts, etc. have been developed and studied as the catalysts for RWGS reaction, but these catalysts were proven to be defective under

certain circumstances (the details would be discussed in section 2.3 catalysts for reverse water gas shift reaction). The objective of this project is to develop the suitable nanomaterial-based catalyst by Reverse Microemulsion method (RME) which exhibit high selectivity to CO while maintaining high activity and good stability for the RWGS reaction. Based on the critical analysis of the literature, Molybdenum-based catalyst were suggested as potential formulations for the RWGS reaction.

The specific goals related to the project objective are listed as follows:

1. Evaluate the catalyst performance in terms of CO_2 conversion, CO generation selectivity and stability over the range of temperatures, space velocities and other relevant operating conditions.
2. Conducting catalytic performance evaluation of the corresponding metal oxides to investigate the effects of carburization (converting oxide to carbide) on the catalyst activity, selectivity, and stability.
3. Conducting catalytic performance evaluation comparison between the corresponding catalysts synthesized by Reverse Microemulsion method and Reverse Microemulsion-Wet Impregnation method (RME-WI) to investigate the effects of preparation methods on the catalyst activity, selectivity, and stability.
4. Conducting catalyst characterization using analytical techniques (XRD, TEM etc.) and temperature programmed reactions to deduce possible reaction mechanisms.

The expected contributions of this thesis is to develop the high surface area molybdenum carbide nanomaterials-based catalyst by Reverse Microemulsion method (RME), which exhibit superior catalytic performance while maintaining complete selectivity to CO and good stability for the RWGS reaction.

1.3 Thesis Outline

This thesis consisted of the study on the Mo-catalysts synthesized by Reverse Microemulsion method (MoOx/γ-Al_2O_3 and Mo_2C/γ-Al_2O_3 denoted as "MoOx(RME)" and "Mo_2C(RME)" throughout the text) and the Mo-catalysts synthesized by Reverse Microemulsion – Wet Impregnation method (MoOx/γ-Al_2O_3 and Mo_2C/γ-Al_2O_3 denoted as "Mo_2C(RME-WI)" and "MoOx(RME-WI)" throughout the text). Thesis chapters are summarized as follows:

Chapter 2 introduces the background and reviews past and recent literature on RWGS catalysts and reverse microemulsion method. Chapter 3 describes all analytical techniques used in this project with schematics. Chapter 4 presents the methodology for the catalytic performance evaluation, including catalyst preparation, experimental flow system setup, experiment design, and data processing.

Chapter 5, 6 and 7 include the experimental results of the catalytic performance evaluation, catalyst characterization results, conclusion drawn from the analyzed data and future directions. The results of the catalytic performance evaluation over various reaction conditions and stability test are shown and discussed in Chapter 5. Chapter 6 focuses on the catalyst characterization conducted by ICP-MS, SEM-EDS, TPR, TEM, XRD, TGA-FTIR and some other catalyst characterization results. These results were analyzed leading to the discussion on reaction mechanisms, including activity, selectivity, and stability. Chapter 7 concludes the results obtained and discusses future direction related to the project.

Chapter 2

Background and Literature Review

2.1 CO_2 emission and global climate change

The dynamic exchange between terrestrial with combination of aquatic environments and the atmosphere generally build up the natural carbon-cycle of CO_2. The estimation of carbon dioxide content in the Earth's atmospheric is 750 Gt of carbon, while the exchange of carbon between the atmosphere and ocean is equivalent to approximate 90 Gt of carbon per year and terrestrial biosphere, including the plants, microorganism and underground inorganication, stores amounts corresponding to ca. 90 Gt globally per year. Such carbon uptake in terrestrial biosphere is balanced by the carbon emission in the form of carbon dioxide generated from the respiration activities of animals and plants, and natural emissions of volcanoes. Human activities emits the amount of CO_2, which is estimated at 5.5 Gt carbon per year. However, the total anthropogenic carbon emissions could be estimated at 25.7 Gt CO_2 per year (such as the indirect human-caused effects), that represents an approximate 3.9% excess with corresponding to the annual CO_2-flow in the natural carbon-cycle. Such an amount is unbalanced and, as a result, the concentration of carbon dioxide in the atmosphere has been continued to climb steadily over the last tens of years, rising to 415 ppm from ca. 315 ppm [19].

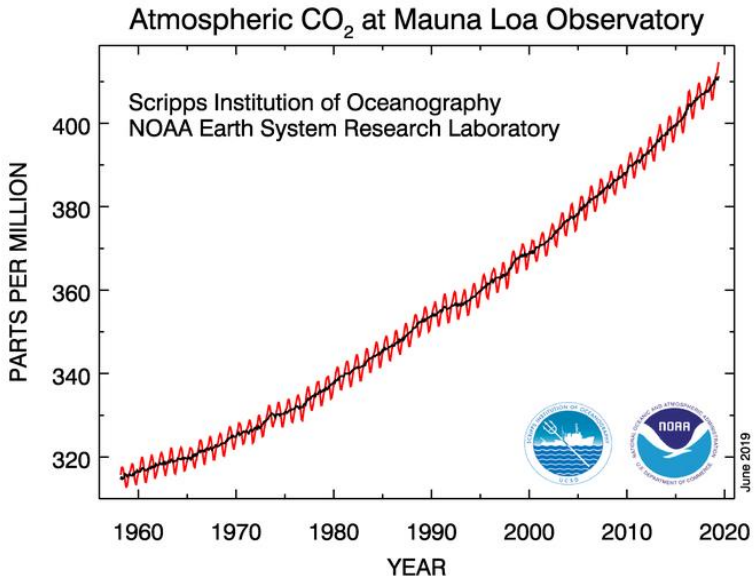

Fig. 1. Changes in concentration of atmospheric CO_2. [13]

The changes in concentration of atmosphere carbon dioxide measured in dry air at Mauna Loa Observatory. Figure 1 showed the longest record of concentration of CO_2 measured directly in the atmosphere.

Only an average 32% of the carbon-related chemical energy content (fossil and provided from the biosphere) utilized in human activities is transformed into and used as multiple types of energy (mechanical, electric, etc.), while the remaining 68% is lost as heat transferred to atmosphere causing its thermal destabilization. The release of heat to the atmosphere causes a high water vapor pressure, in turn, heavy precipitations. The impact is added to this direct warming owning to the increased concentration of carbon dioxide and other greenhouse gases (GHGs), including water vapor, which prevents the infrared radiation emitted by the surface of the earth escape to the troposphere during the night. The "atmospheric warming" associated with global climate change and planetary temperature increase is considered as a consequence caused by these two combined effects. Although fluctuation of the temperature is constant in the history of

our planet, it is a fact that peaks cause dramatic events. Therefore, it is imperative to avoid large increase of temperature, decreasing the release of thermal energy to the atmosphere and stopping CO_2 accumulation [20].

Canada's emissions profile is similar to that of most industrialized countries, in that CO_2 is the largest contributor to total emissions, accounting for 79% of total emissions in 2016 as shown in Figure 2. The majority of the CO_2 emissions in Canada result from the combustion of fossil fuels [21].

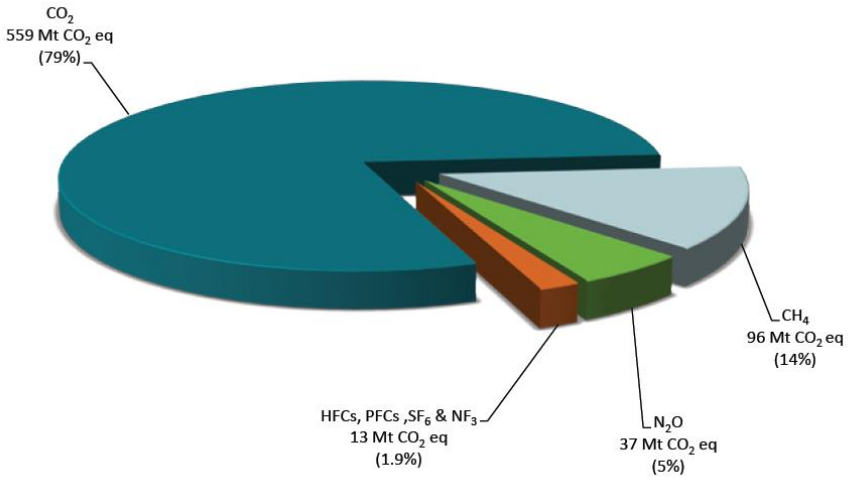

Fig. 2. Canada's GHG emission (2016). [21]

In 2016, the Energy-Stationary Combustion emitted 45% of Canada's total GHG emissions while the Waste and Industrial Processes emitted approximately 10% of Canada's total GHG emissions as shown in Figure 3. Compared with other sources, such as Energy-Transport source, it's feasible to capture carbon dioxide emissions from Energy-Stationary Combustion, Waste and Industrial Processes sources [21].

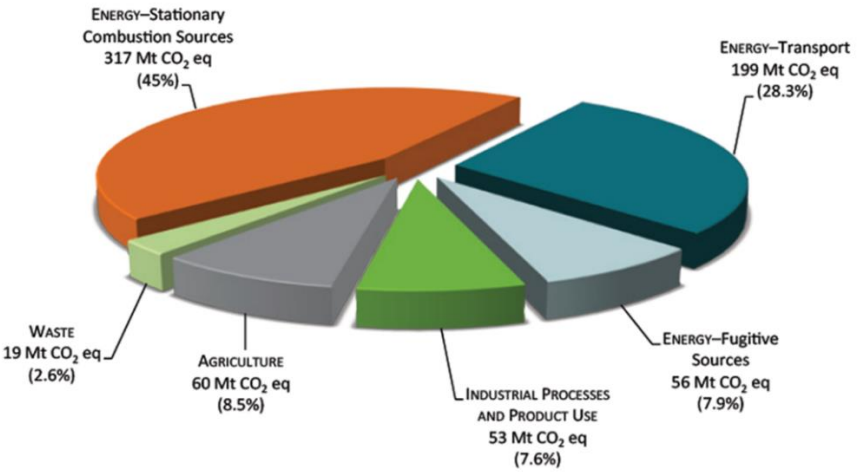

Fig. 3. Canada's GHG emission (2016). [21]

Electricity generation is shown in Figure 4 by source in Canada in 2016 with total electricity generation of 648 terawatt hours. Hydro sector has the most notable portion of generation at 59%. 15% of electricity was generated from nuclear, while 7% was produced by non-hydro renewables. The remaining electricity were generated by gas/oil/others at 10% and coal at 9% [22].

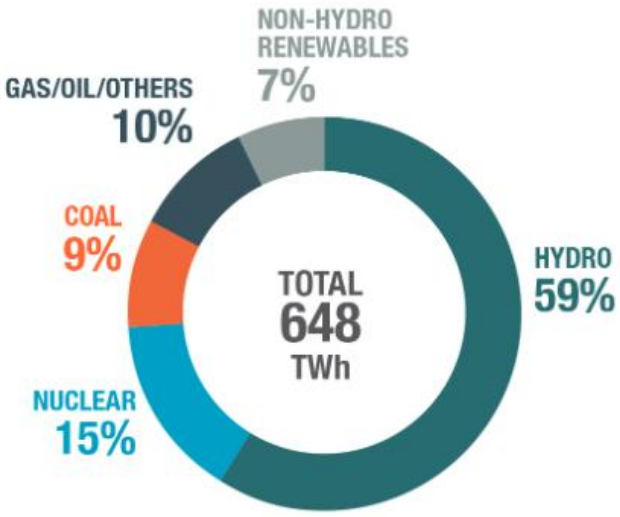

Fig. 4. Electricity generation by source in Canada (2016). [22]

The need to significantly reduce the CO_2 emissions has become more urgent as atmospheric carbon dioxide concentrations have continued to increase. To deal with the carbon dioxide emissions, several promising approaches would be introduced and discussed.

2.2 Thermocatalytic conversion of CO_2

2.2.1 Reaction pathways

Although CO_2 is an environmentally unfriendly GHG, non-flammable, non-corrosive, no toxic and abundant nature of carbon dioxide make this chemical as an ideal reactant. Abundant resources, including emissions from power plants and industrial processes, landfill gas and biogas provide the feasibility of various approaches.

Converting CO_2 captured into synthetic valuable fuels and useful chemicals is a promising route for reduction of CO_2 emissions. Therefore, many research groups put effort into this topic, focusing on photochemical and electrochemical reduction of CO_2 into various products. Photocatalytic reduction of carbon dioxide is attractive since it just utilizes H_2O and CO_2 as the reactants and the sun or electricity generated from renewable energy as a source of energy. However, the solar energy utilization restricts the photochemical CO_2 reduction, while low efficiencies of electricity utilization restrains the electrochemical reduction of CO_2. Both processes have transport limitations and are restricted by the low CO_2 solubility in water at low temperatures. Thermocatalytic conversion is an alternative approach.

Three main approaches have been proved to be effective and promising routes to reduce the concentration of atmospheric CO_2: direct CO_2 emission reduction, CO_2

capture and storage (CCS), and CO_2 capture and utilization (CCU) through conversion into synthetic chemicals and fuels [23]. Direct reduction of CO_2 emissions is based primarily on improving the efficiency of fossil fuel utilization. It is difficult to reduce the carbon dioxide emissions through this path due to the rapidly increasing population and growing demand for high quality of life in developing countries. Limited capacity due to high capital, operating costs and unknown consequence of long-term storage are considered as the challenge of reducing carbon dioxide emissions through CO_2 capture and storage, e.g., in geological formations.

CO_2 capture and utilization for further development of synthetic fuels and useful chemicals using renewable energy is of particular interest as this technology allows for creating an artificial carbon cycle.

Hydrogen (H_2) is required for the conversion of CO_2 into synthetic fuels and useful chemicals. In actuality, hydrogen is the most abundant element in the Universe; oxygen is third and carbon is forth. In addition, simple molecules, such as carbon dioxide (CO_2), water (H_2O) and methane (CH_4), are composed of these basic elements. There is a large amount of water on Earth that could be utilized to generate H_2 for CO_2 hydrogenation. However, considering water (H_2O) is a highly oxidized compound, energy is required for generating H_2 from H_2O that could be provided by renewable sources, such as hydro, wind and solar. Such promising process that H_2 was separated from H_2O by using renewable energy and further used for conversion of carbon dioxide will create a path for the generation of renewable synthetic fuels from CO_2. In other words, intermittent renewable energy could be stored in a chemical form. Eventually, an artificial carbon cycle could be created by the large-scale thermocatalytic conversion of CO_2 in combination with the utilization of renewable H_2, recycling the carbon dioxide emitted in our energy distribution systems in order to reduce the consumption

of unsustainable energy.

A number of remarkable pathways for thermocatalytic conversion of CO_2 as shown in Figure 5, red and blue arrows presenting exothermic and endothermic processes respectively.

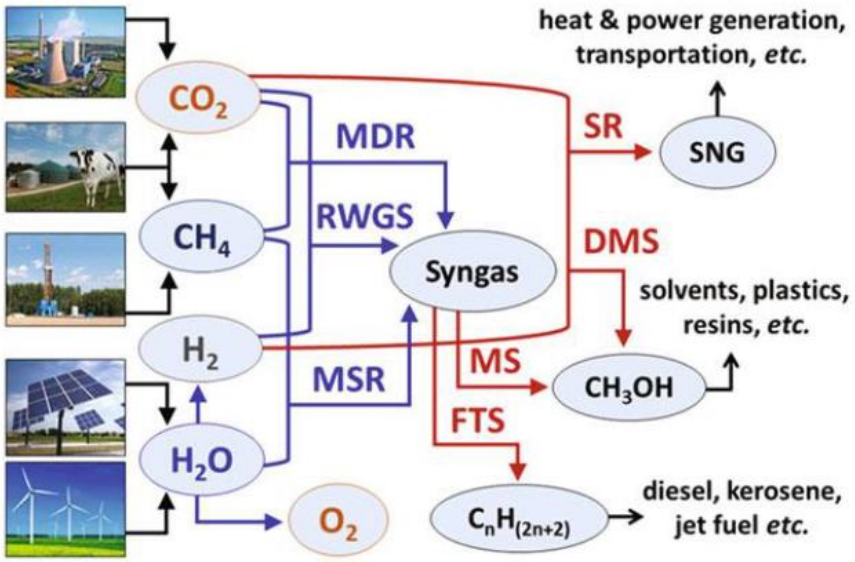

Fig. 5. Reaction pathways of producing synthetic fuels and chemicals from CO_2. [23]

Syngas, synthesis gas, is a gas mixture comprising of primarily hydrogen (H_2), carbon monoxide (CO) and very often some carbon dioxide (CO_2). Syngas could be produced by a process of methane steam reforming (MSR) which is the reaction of methane (CH_4) and water or methane dry reforming (MDR) which is the reaction of methane and carbon dioxide. Reverse water gas shift reaction (RWGS) is another promising avenue for CO_2 hydrogenation to generate syngas by combining carbon dioxide and hydrogen. Direct methanol synthesis (DMS) is a notable process combining CO_2 and H_2 to generate methanol. Another pathway for thermocatalytic CO_2 conversion is Sabatier reaction (SR, also known as CO_2 methanation) which is the highly

exothermic reaction. CO_2 methanation could generate synthetic CH_4, frequently referred to as renewable natural gas (RNG) or synthetic natural gas (SNG). Syngas is a valuable raw material in industrial processes. Several feasible options are existed for the further development of valuable synthetic chemicals in relation to the different H_2/CO ratio of syngas as shown in Figure 6 [24]. Syngas could be further converted into ethanol, various useful chemicals via methanol synthesis (MS) and fuels via Fischer-Tropsch synthesis (FTS). Additional, syngas could be used to produce hydrogen and used for power generation.

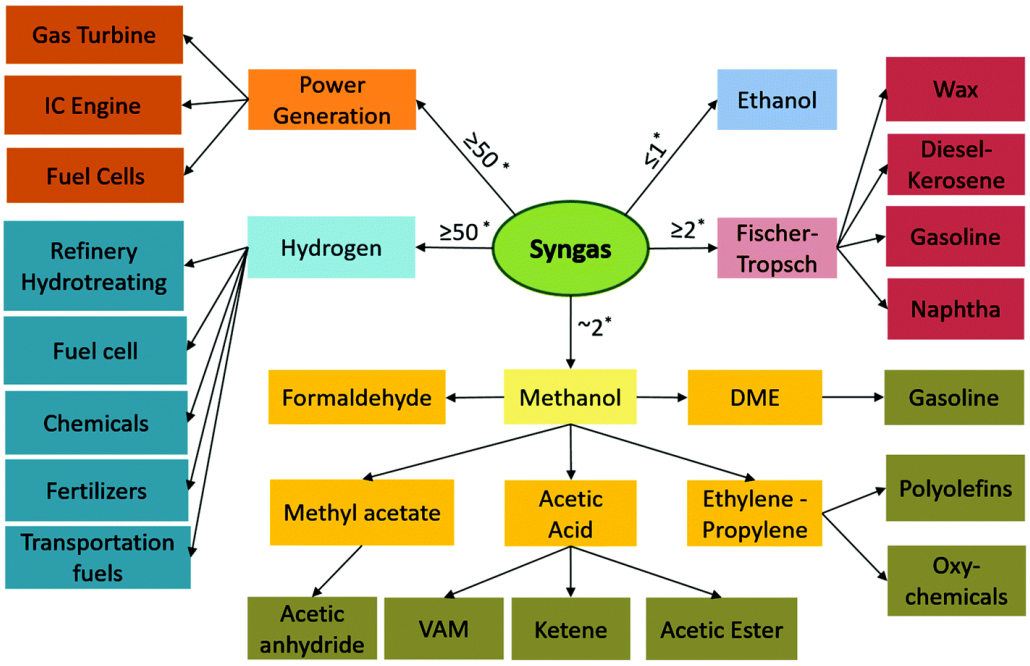

Fig. 6. Syngas derivatives. [24]

In this project, reverse water gas shift reaction (RWGS) has been focused on which could generate syngas for further developments.

2.2.2 Reverse water gas shift

The RWGS reaction was considered as a key step in the utilization of CO_2 and estimated to be a more efficient way to produce liquid fuels as the process can be integrated with current technologies for thermocatalytic conversions [25]. In order to achieve high conversion for the RWGS reaction, it should optimally be run at high temperatures which is attributable to the endothermic reaction. At higher temperatures, however, the reaction is limited by deactivation due to coking and sintering. The equilibrium can be shifted towards CO formation by changing feed composition. At high H_2:CO_2 feed ratios, more CO_2 is consumed; though this approach increases the operational cost associated with separation of H_2 from the product stream [26]. Other alternatives to shift the equilibrium include selective removal of the water being formed by using a desiccant bed or a membrane permselective to water [10].

2.3 Catalysts for reverse water gas shift reaction

The reverse water gas shift reaction studies of supported metal catalysts mainly compose of noble metal (Pt, Rh and Pd) immobilized on various supports. Furthermore, a wide variety of metals have attracted widespread attention.

2.3.1 Noble metal catalysts

Noble metals (Pt, Pd, Rh and Ru) have excellent activity and superior resistance against sintering and coking [27]. It has been found that supported metal catalysts such as Pt, Pd, and Rh immobilized on various supports such as Al_2O_3, ZrO_2, TiO_2, and CeO_2 are active for the RWGS reaction. However, due to the relatively high loadings of noble metal (usually 1-5 wt.%), the cost associated with current platinum group metal-based catalysts is prohibitively high. 1 wt.% Pt/TiO_2 achieved around 20% CO_2 conversion with 95% selectivity to CO at a 50ml/min feed gas flow with CO_2:H_2:N_2 = 45:45:10 at 400°C. The active sites for the CO production were identified as Pt-O_v-Ti^{3+} species

formed at the interface between Pt and reducible TiO_2 support, while large Pt particles facilitate the CH_4 formation at high temperatures [28]. Even though Pt/CeO_2 systems have shown to achieve high conversion, poisoning of Pt by CO have been observed[29]. Goguet et al. demonstrated that increasing carbon deposition on catalyst surface are caused by high CO concentration for 2% Pt/CeO_2 catalyst [29].

2.3.2 Cu-based catalysts

Currently, some catalysts used in water gas shift reaction (WGS) are used in reverse water gas shift reaction (RWGS) as well considering the reversibility of the reaction. Commonly used catalysts for water gas shift reaction, i.e. Cu-based catalysts, provided promising catalytic performance. As such, this catalyst has been extensively studied. Cu-based catalysts could catalyze both the forward and reverse water-gas shift reactions [30-32]. Two major advantages of the use of Cu for RWGS are indicated: (i) at low temperatures (~ 165°C) it has been shown to perform RWGS [33] and (ii) minor or no methane is formed as a byproduct [31, 32, 34]. For the 40wt% $Cu/ZnO/Al_2O_3$ catalyst, 17% CO_2 conversion with complete selectivity to CO was achieved at 500°C GHSV = 90,000 mL/ (g h), $H_2:CO_2 = 4$, pressure = 3 bar. Regarding catalyst stability, the catalyst bed was completely clogged after 25 h on stream at 700°C GHSV = 85,000 mL/(g h), $H_2:CO_2 = 4$, pressure = 3 bar [34]. However, without hydrogen, CO_2 dissociation is highly unfavorable on clean Cu surfaces [35-37] and coking and sintering occur significantly at higher temperatures [38].

Not only the amount of active sites but also the catalysts' nature, such as, the size and shape-dependent have a strong effect on the general catalytic activity [39-42]. Therefore, innovative approaches were investigated which could potentially provide superior activity and stability and give many degrees of freedom, including the implementation of cheaper emerging materials, such as bi- and multi-metallic alloys.

transition metal oxides and nano-carbides.

2.3.3 Catalysts based on transition metal oxides

Transition metal carbides are an attractive, low cost alternative, as their surfaces have electronic configurations similar to those of some precious metals, providing high catalytic activity in water gas shift reaction [43] [44]. Molybdenum carbide (Mo_2C) is of particular interest due to its dual functionality for H_2 dissociation and CO_2 scission [45]. Mo_2C has been recently studied as a catalyst for the RWGS reaction [45-47]. The performance of the Mo_2C catalyst prepared by carburizing in C_2H_4 at 700 K in the RWGS reaction was found to be superior to Pt and Pd in terms of both conversion and selectivity [45]. In another study, Mo_2C nanowires synthesized via calcining the ammonium heptamolybdate/aniline co-precipitate provided CO_2 conversion greater than 60% at 873 K and GHSV of 36,000 ml/(g h). The catalyst presented 100% selectivity to CO at H_2:CO_2 molar ratio of 4. The selectivity to CO production was maintained for 20 h at 873 K at a space velocity of 240,000 ml/(g h) and H_2:CO_2 molar ratio of 1, although the conversion dropped to 28% [46]. While these recent findings are promising, further investigation is necessary to evaluate the applicability of Mo_2C as a catalyst for the RWGS reaction. In particular, it is required to study in more detail the Mo_2C-catalyzed RWGS reaction at high CO_2 conversions, which is more relevant to industrial applications. Recent studies mainly focus on the low temperature range when CO_2 conversion is less than 30% [47].

2.3.4 Support effects

Sakurai et al.[48] synthesized and evaluated the Au nanoparticles supported on ZnO, Fe_2O_3, Al_2O_3 and TiO_2 at two distinct pressures (P = 1 and 50 bar). TiO_2 showed the most superior activity under both reaction conditions. Fe_2O_3 and Al_2O_3 maintained high activity at 1 bar as well however it significantly decreased at 50 bar, whereas ZnO

exhibited a low activity under both test conditions.

2.4 Reverse microemulsion method for catalyst preparation

The nanomaterials synthesis has received considerable attention in recent decades since the discovery of microemulsions by Jack H. Shulman in 1959, considering nanoparticles maintain unique physical and chemical properties [49]. Synthesis of nanoparticles by microemulsion method is an area of considerable current interest. The reverse microemulsion (RME) preparation method has been proved to be a promising and effective technological application in abundant areas such as microelectronic devices [50], photocatalysis[51], biomedical applications [52], which allows in some cases to control the nanoparticle properties such as particle size distribution, morphology.

Microemulsion is an isotropic, transparent (or translucent), thermodynamically stable liquid mixture of oil, water and surfactant, frequently in combination with a cosurfactant, which could be generally classified as oil-in-water (o/w) and water-in-oil (w/o). IUPAC defines micro-emulsion as dispersion made up of water, oil, surfactant(s) and cosurfactant that is an isotropic and thermodynamically stable system with dispersed domain diameter ranging approximately from 1 to 100 nm, usually 10 to 50 nm [53].

The complex film is formed due to surfactant and co-surfactant together at the interface of oil and water and, therefore, the generation of microemulsion droplets occurs [54]. The water-in-oil microemulsion (reverse microemulsion) is topologically similar to reverse micelles [55] (where the polar heads of the surfactants and cosurfactant are oriented inward while the non-polar tails orienting towards the oil continuum.). The difference is addressed as follows: the compositions that yield a rigid

interior (or core) by immobilizing the water present in a way of hydration of the polar heads of the surfactants and cosurfactants (when present) are referred to as ‘reverse micelles’; compositions exist mobile or free water in the core after satisfying the hydration requirements of head groups of surfactants and cosurfactants (when present) are called ‘microemulsions’[56]. The free water existing in the core could be considered as the ‘nano-pool’. Illustrative representations of reverse micelles and microemulsions are presented in Figure 7.

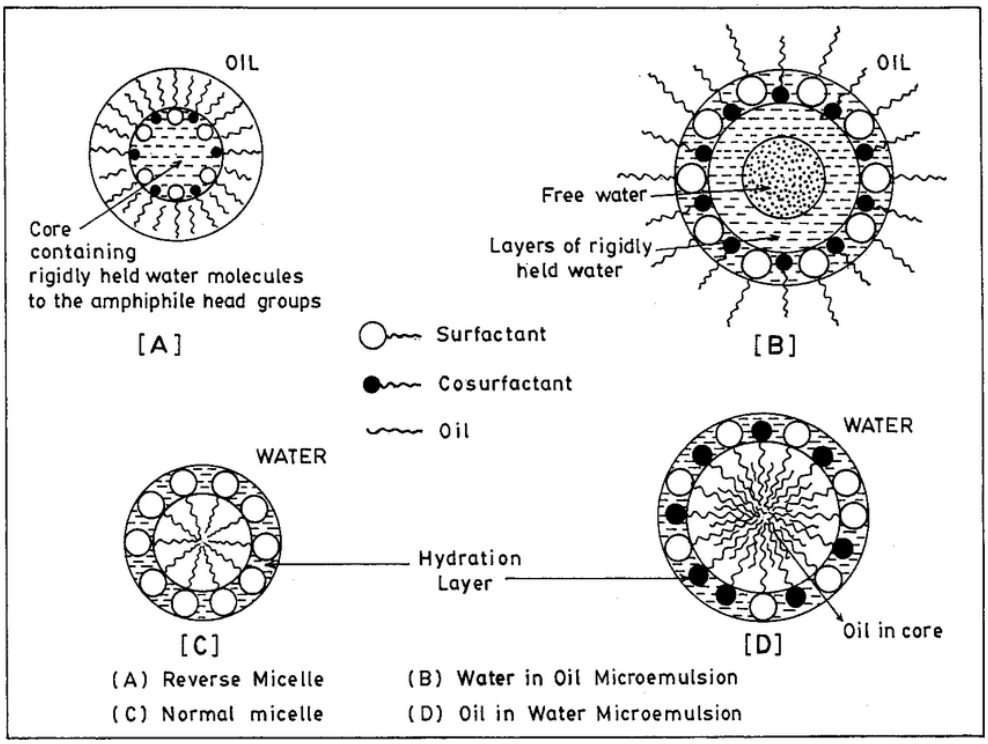

Fig. 7. Pictorial representations of reverse micelles and microemulsions. [56]

Reverse microemulsion method is commonly used to synthesize nanoparticles to avoid broad particle size distributions that usually result from precipitation. A relatively novel approach of using microemulsions to prepare the nanoparticles is in a way of multi-microemulsion. This route involves multiple sets of microemulsions with the identical water, oil, surfactant and cosurfactant used and similar ratios of the four

components but with the aqueous phase of different microemulsions containing each of the reactants for the nanoparticles [57]. Intermicellar exchange of reactants existing in the different ‘nano-pools’ subsequently occurs with carrying out the chemical reactions and the nanoparticles form as shown in figure 8. Studies demonstrated that “the multi-microemulsion route could generate finer particles and narrow particle size distributions [58].

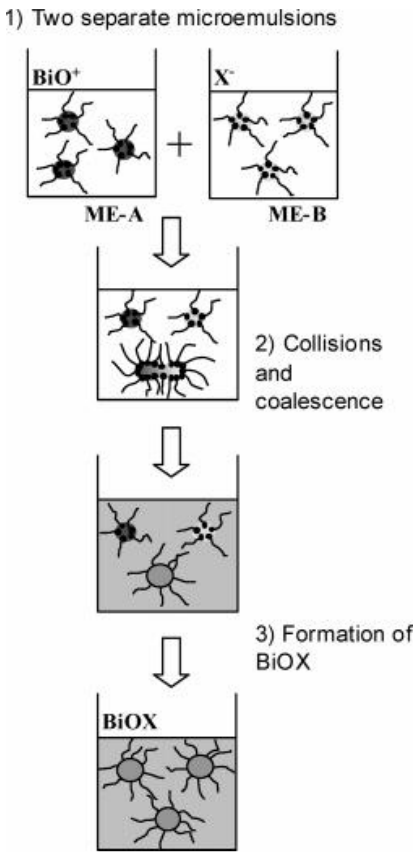

Fig. 8. Multi-microemulsions route of synthesizing nanoparticles. [58]

In order to overcome the challenge that the activity of catalysts is limited by low surface area , this novel preparation method is introduced to synthesize high surface area nanomaterials. The ultimate objective is to develop a catalyst which exhibits superior catalytic performance while maintaining complete selectivity to CO and good stability.

Chapter 3

Methodology

In this chapter, all analytical techniques used in this study are briefly presented with fundamental principles and schematics, which are generally standard methodologies to investigate the catalysts composition, morphology and crystalline structure.

3.1 X-ray powder diffraction (XRD)

X-ray powder diffraction (XRD) is an analytical technique that could identify the phase of a crystalline material and provide detailed information about physical properties, chemical composition and the crystalline structure. Considering that the wavelength of X-rays is similar to the distance between atoms in the crystal (10-8 cm), crystals can be seen as diffraction gratings for X-rays [59].

X-ray diffraction is based on constructive interference of monochromatic X-rays and a crystalline sample. A cathode ray tube could generate the monochromatic X-rays and produce monochromatic radiation after filtration. After being collimated to concentrate, these X-rays directed toward the sample. Constructive interference was produced due to the interaction of sample and the incident rays when conditions satisfy Brag's law: $2d\sin\theta=n\lambda$ where λ is the wavelength of the X-ray, n is any positive integer, d is plane spacing and θ is the grazing angle. The crystal structure can be determined by analyzing the diffraction pattern obtained on the photographic film. When X-rays are under the condition of the above equation, the superposition will be obtained on the direction of reflection. If the direction θ of the diffraction wave is first measured for a known crystal, the wavelength of the X-ray can be calculated to determine the element that produces the characteristic X-ray.

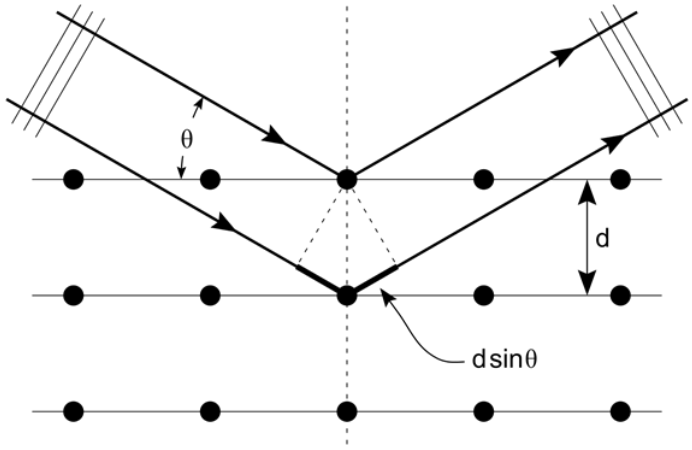

Fig. 9. Bragg diffraction. [59]

3.2 Inductively coupled plasma optical emission spectrometry (ICP-OES)

An atom or ion can be in a discontinuous state of energy. When an atom or ion in the ground state absorbs a certain amount of external energy, its extranuclear electrons transition from an energy state to a higher energy level orbit. The atoms or ions in the excited state are very unstable. After 10-8 seconds, they will transition to the ground state and radiate the absorbed energy with a certain electromagnetic wave. The electromagnetic waves are arranged in a certain wavelength for different atoms. Since atoms or ions have many energy levels and the structures of different elements are different, a particular spectrum of atoms or ions can produce a series of characteristic spectra of different wavelengths which will give the element information [60]. The intensity of the wave at different wavelengths can be used to quantitatively analyze the content or concentration of an element in the sample after comparison with the standard curve.

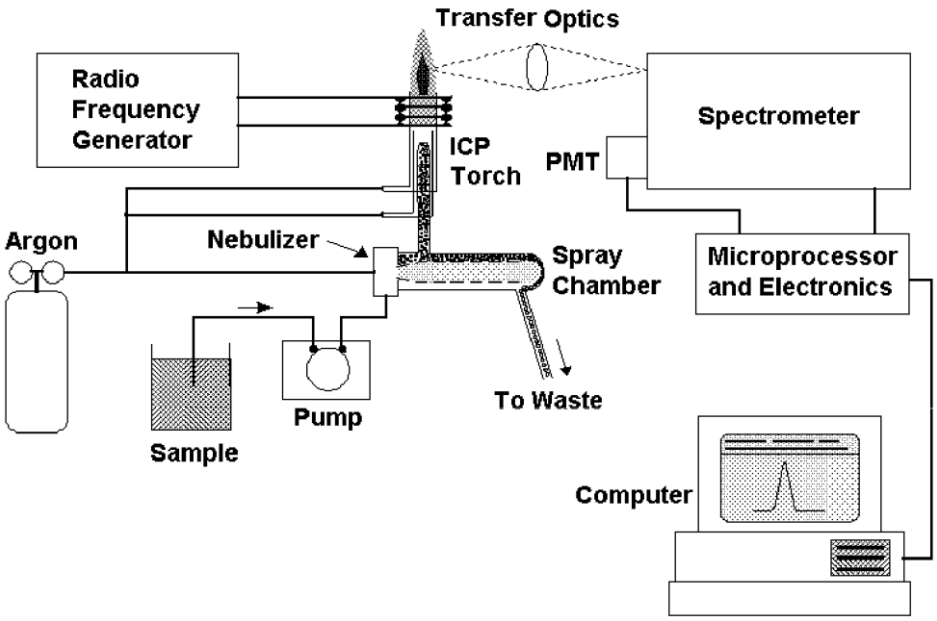

Fig. 10. Major components and layout of an ICP-OES instrument. [60]

3.3 BET Surface area analysis (SAA)

Surface area analysis is based on the BET (Brunauer–Emmett–Teller) theory which describe the adsorption of gas molecules on the solid surface to evaluate the specific surface and pore distribution of the powder sample according to the amount of adsorption usually by a TCD detector. At a constant temperature, equilibrium state, a certain gas pressure corresponds to a certain amount of gas adsorption on the solid surface and changing the pressure will affect the adsorption amount. When the sample is immersed in liquid nitrogen, gas nitrogen molecules that are passing through the sample will be physical adsorbed on the catalyst surface (chemical adsorption is avoid at low temperature). When the liquid nitrogen is removed, temperature raise up and nitrogen will desorb, and a negative peak will occur. The amount of adsorbed and desorbed molecules can be calculated by the area of the peaks [61].

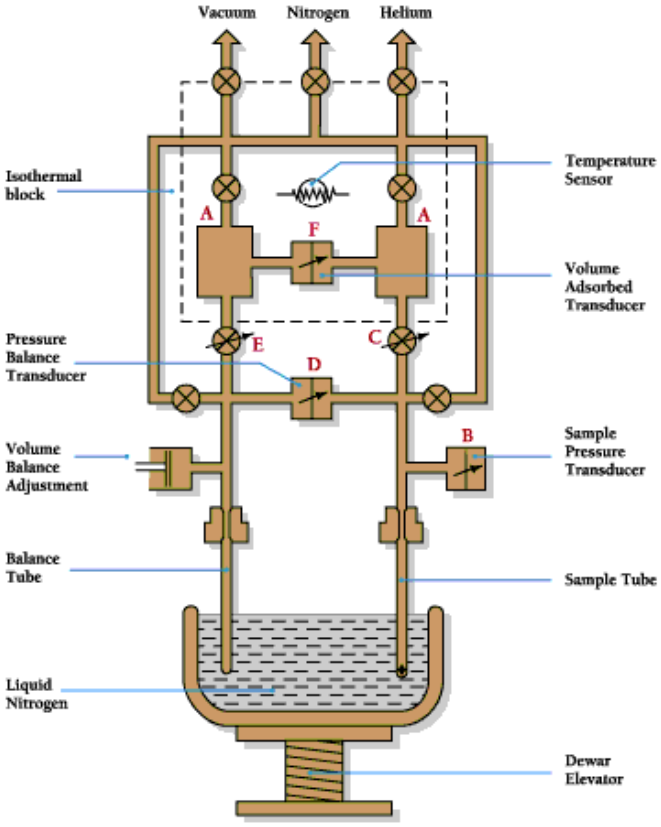

Fig. 11. Major components and layout of a BET surface area analyzer. [61]

BET model can be described by the following equation, where P is the pressure at equilibrium, P_0 is the saturated vapor pressure of the adsorbed gas at this temperature, V_m is the volume of gas required to form a monolayer on the surface, V is the amount of adsorption when the pressure is P, C is a constant.

After a series of p and V is obtained, $p/V(p_2-p)$ is plotted against p/p_2 plot, a straight line can be obtained. The slope of the line is $(C-1) / CV_m$ and the intercept is $1 / CV_m$ so that V_m and constant C can be deduced. Using the surface area equation, the specific surface area can be obtained. Where N_A is the Avogadro constant, s is the adsorption cross-sectional area of the adsorbed species, V is the molar volume of the adsorbed species and a is the quality of the adsorbent material.

$$\frac{P}{V(p_2 - p)} = \frac{1}{V_m C} + \frac{C-1}{V_m C} \times \frac{p}{p_2} \quad (6a)$$

$$S_{total} = \frac{(V_m N_A s)}{V} \quad (6b)$$

$$S_{BET} = \frac{S_{total}}{a} \quad (6c)$$

3.4 Scanning Electron Microscope (SEM) and SEM-EDS

Scanning Electron Microscope (SEM) is an electron microscope developed after transmission electron microscopy. A focused electron beam is generated form the source and scan the surface of the sample point-by-point. After interacting with the sample, various physical signals are produced, amplified, and converted into modulated signals by the detector, and finally displayed on the screen to present various features of the sample. SEM is strong in generating stereoscopic images, has large magnification range, allows continuous adjustment, has high resolution and is simple to prepare the sample. It is an effective tool for surface investigation [62].

The combination of SEM and energy dispersive X-ray spectroscope is often used to analysis the dispersion of the elements on the sample surface and EDS will provided the element distribution and create a mapping for each element. This combination allows connecting the SEM spectrum and the dispersion of a component of the elements.

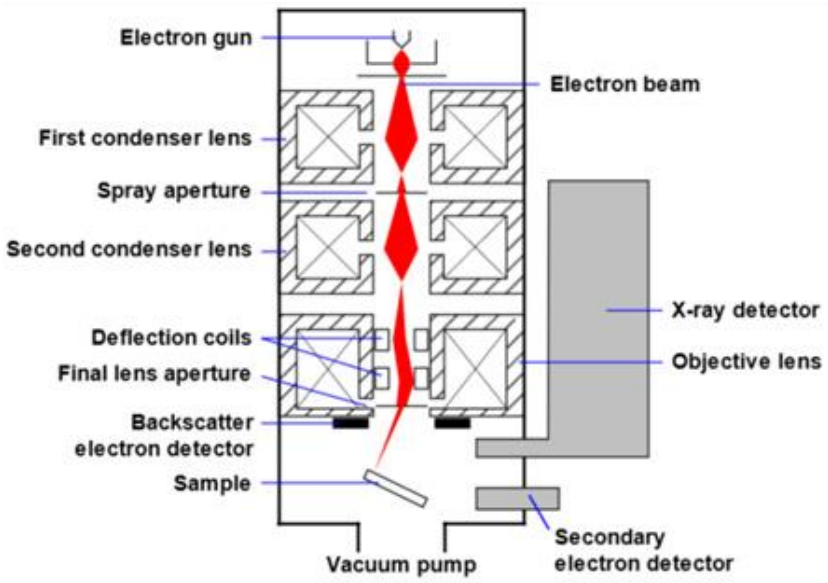

Fig. 12. Schematic of a Scanning Electron Microscope. [62]

3.5 Transmission electron microscopy (TEM)

Transmission electron microscopy is a high resolution electro-optical instrument that the transmitted focused electrons transmit the sample to generate image using an extremely short wavelength electron beam as the source. The most advanced TEM has a resolution of 1 nm and can be used to directly observe atomic images. Since the spectrum is generated by transmission, the thickness of the sample should be ultrathin that the signal can go through and there is only one layer of the sample [63]. The TEM consists of an electro-optical system, a power supply and control system, and a vacuum system. When the electron beam passes through the sample, the transmitted electrons have different structure strength and appearance information, showing different strengths. After the signal being processed and magnified, it is focused on a photographic screen.

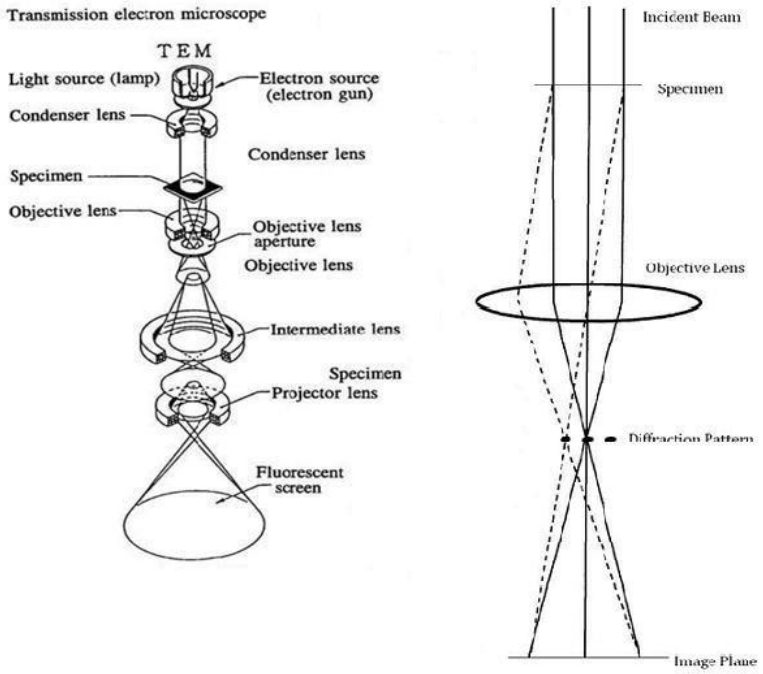

Fig. 13. General layout of a TEM (left). A ray diagram for the diffraction (right). [63]

3.6 Temperature-programmed reduction (TPR)

Temperature programmed reduction (TPR) method is one of the temperature programmed analysis methods. In the TPR experiment, a certain amount of metal catalyst is placed in a fixed bed reactor, and a reducing gas stream (usually a low concentration hydrogen) is passed through the catalyst at a certain flow rate while heating the reactor at a certain rate. When the temperature reaches a certain value, the oxide on the catalyst begins to be reduced. Because the flow rate of the reducing gas is constant, the change in H_2 concentration after passing through the catalyst bed is proportional to the reduction amount of the catalyst.

The change of H_2 concentration is continuously detected by a gas thermal conductivity detector (TCD detector), and the curve was recorded to obtain a TPR spectrum of the catalyst. Each TPR peak in the figure generally represents a reducible

species or state in the catalyst, and the area under the curve is proportional to the amount of the oxide species. Information on the change of metal state, the interaction between two metals, the interaction between metal oxide and support, and the activation energy of oxide reduction reaction can be deduced by TPR results [64].

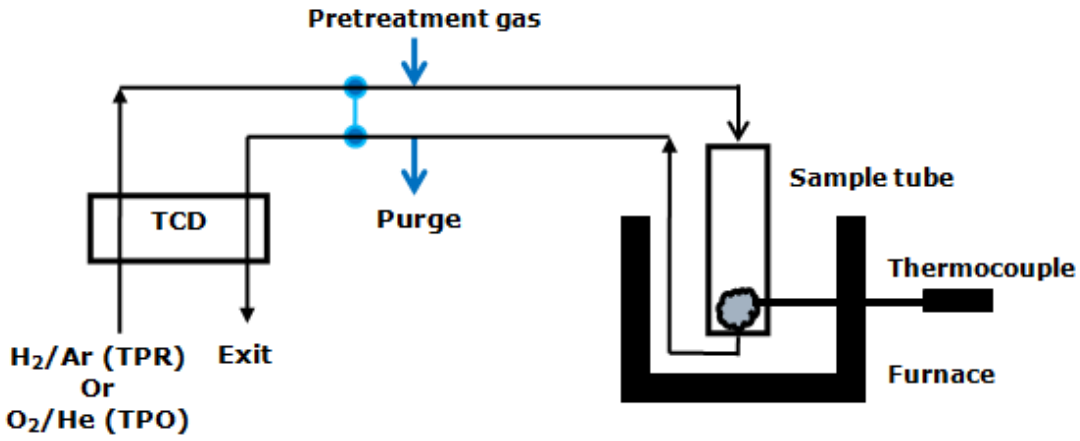

Fig. 14. Schematic diagram for TPR/TPO analysis. [64]

3.7 Thermogravimetric Analysis (TGA)

Thermogravimetric Analysis (TGA) is a thermal analysis technique that measures the relationship between mass and temperature of the sample that is heated at a certain ramping rate, to study the thermal stability and composition of the material. By analyzing the thermogravimetric curve, the temperature composition of the weight changing, and its intermediates, thermal stability, thermal decomposition, and product formation can be deduced. Thermogravimetric method is favoured by its high quantitative ability to measure the mass change and rate of change of a substance accurately. Processes that all have mass change can be recorded and analyzed by TGA, such as sublimation, vaporization, adsorption, desorption, but thermal behaviors such as melting and crystallization, do not involve mass change of the sample, which can not be analyzed by TGA method [65].

In this study, the reaction gas used in TGA is air and the experiments are temperature-programmed oxidation. The system was heated up slowly, and the weight change along with the temperature is recorded. The coking degree of our catalysts after reaction can be analyzed.

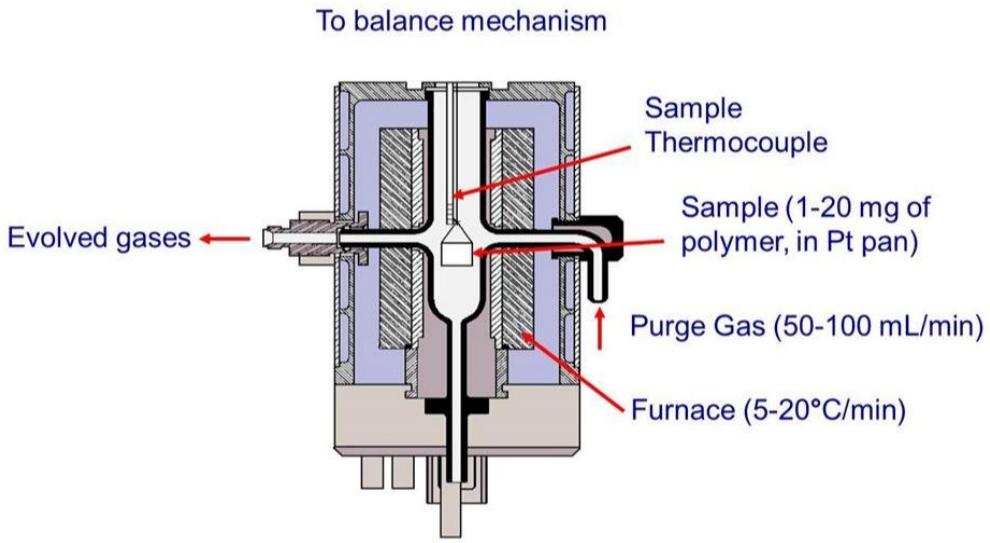

Fig. 15. Schematic diagram for TGA. [65]

After introducing the characterization techniques, catalyst synthesis, system setup, data processing and more characterization details are going to be presented in next chapter.

Chapter 4

Experimental Setup

In this chapter, catalyst synthesis, set up of fully automatic flow system for catalytic performance evaluation and data processing are presented. In addition, catalyst characterization techniques are introduced in more details.

4.1 Catalyst synthesis

In this study, 20 wt.% $MoO_3/\gamma\text{-}Al_2O_3$ and 20 wt.% $Mo_2C/\gamma\text{-}Al_2O_3$ were synthesized by two different methods: reverse microemulsion method and reverse microemulsion – wet impregnation method ($Mo_2C/\gamma\text{-}Al_2O_3$ and $MoO_3/\gamma\text{-}Al_2O_3$ synthesized by reverse microemulsion method are denoted as "Mo_2C (RME)" and "MoOx (RME)" throughout the text with $Mo_2C/\gamma\text{-}Al_2O_3$ and $MoO_3/\gamma\text{-}Al_2O_3$ synthesized by reverse microemulsion – wet impregnation method are denoted as "Mo_2C (RME-WI)" and "MoOx (RME-WI)" throughout the text) .

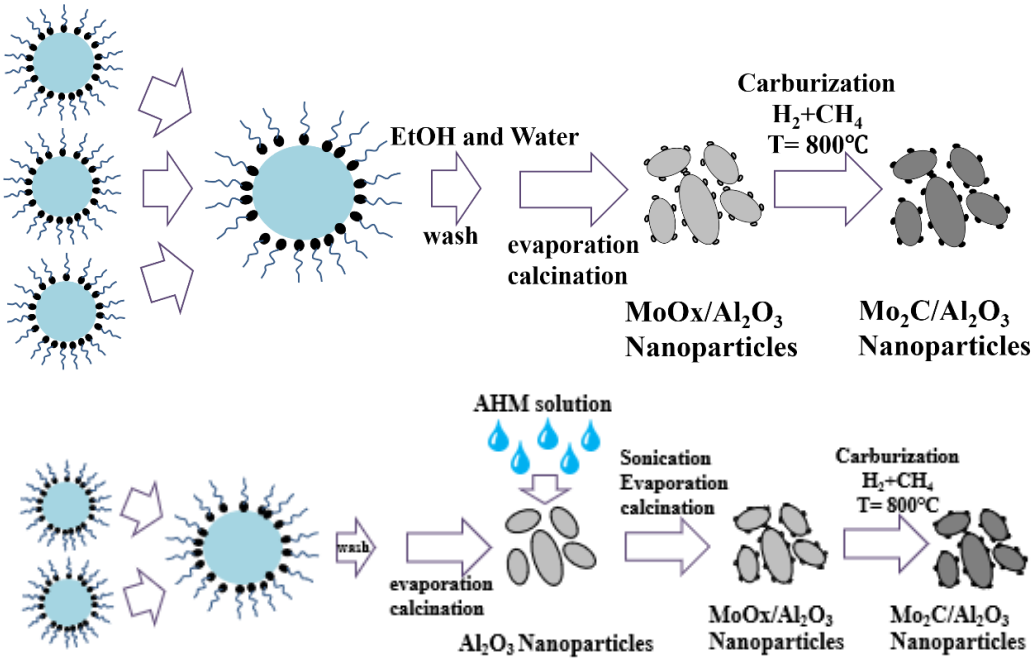

Fig. 16. Process schematic for synthesizing $MoOx/\gamma\text{-}Al_2O_3$ and $Mo_2C/\gamma\text{-}Al_2O_3$ nanoparticles by Reverse Microemulsion method (upper panel) and Reverse Microemulsion – Wet Impregnation method (lower panel).

A non-ionic surfactant Triton X-100 (2-[4-(2,4,4-trimethylpentan-2-yl) phenoxy] ethanol) from Acros Organics was used. Chemicals isopropanol and cyclohexane (C_6H_{12}) were purchased from Sigma-Aldrich. The molybdenum source was ammonium molybdate (VI) tetrahydrate (AHM) from Acros Organics and the alumina source was aluminium nitrate nonahydrate from Acros Organics and ammonium hydroxide from LabChem Inc. Molybdenum oxide supported on alumina nanoparticles was prepared via a three-emulsion method. The microemulsion system consisted of cyclohexane as the continuous oil phase, isopropanol as a cosurfactant, Triton X-100 as a surfactant, and either Mo precursor solution (AHM dissolved in ammonia solution), aluminium nitrate or ammonia solution as the aqueous phases. In these three microemulsion systems as discussed above, the aqueous phases possess the same volume fraction but different volume and compositions while surfactant, cosurfactant and oil phase possess the same volume fraction but different volume as well as indicated in Table 1. The volume of the ammonia solution was in excess as compared with alumina nitrate solution. The three microemulsions were synthesized by mixing (by volume) 10% triton X-100, 35% cyclohexane, 40% isopropanol, and 15% of the aqueous phase separately. In each of the microemulsion systems, a small amount of additional isopropanol was then slowly titrated while stirring until the microemulsion system became transparent. Afterwards, three individual microemulsion were prepared (RME #1: ammonium heptamolybdate tetrahydrate (AHM); RME #2: $Al(NO_3)_3$ RME #3: Ammonia solution). Microemulsion III was then slowly added into microemulsion II mixture with stirring. After 8 hours, microemulsion I was added into the mixture of microemulsion II and III and continued to be stirred. Following sufficient mixing, the microemulsion was allowed to settle and white particles were precipitated. After centrifugation, these particles were separated from the reverse microemulsion and

washed with water and pure ethanol several times to remove remaining chemicals (the ratio of ethanol to water is 3 to 1). The resulting gel-like particles were evaporated at 100°C and calcined at 550°C for 4 hours to produce $MoO_3/\gamma\text{-}Al_2O_3$.

To synthesize $Mo_2C/\gamma\text{-}Al_2O_3$, the $MoO_3/\gamma\text{-}Al_2O_3$ was carburized in a quartz tube under the flow of H_2:CH_4 with a molar ratio of 4:1 (0.5 L/min total flow rate). The heating rate was set to 5 °C/min from room temperature to 250°C and 1°C/min from 150°C to 800°C. The sample was then held at 800°C for 2 hours under the same H_2:CH_4 flow followed by reduction in H_2 (0.5 L/min) for 1 hour followed by cooling down to room temperature under N_2 (0.5 L/min).

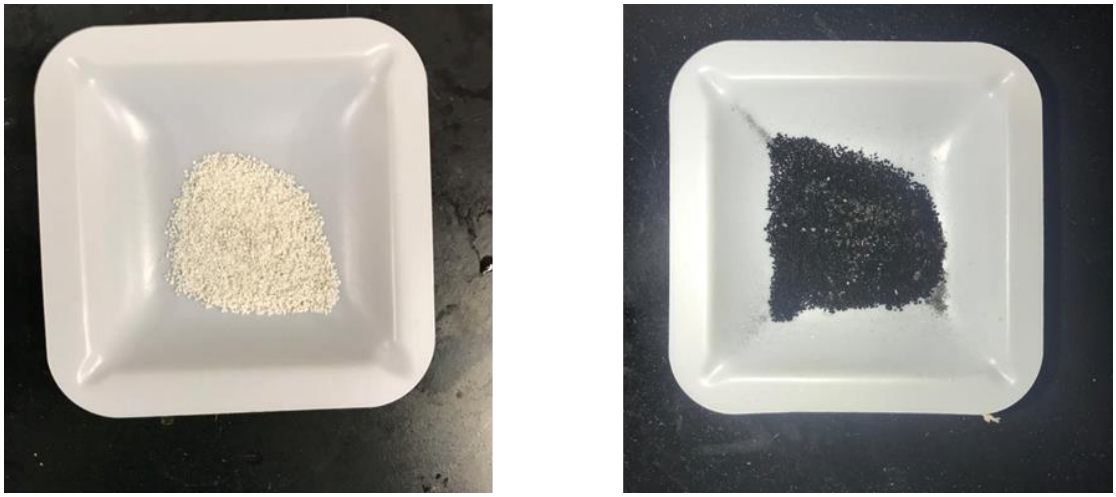

Fig. 17. Pictures of fresh $MoOx/\gamma\text{-}Al_2O_3$ (pelletized) (left) and spent $MoOx/\gamma\text{-}Al_2O_3$ (pelletized) (right).

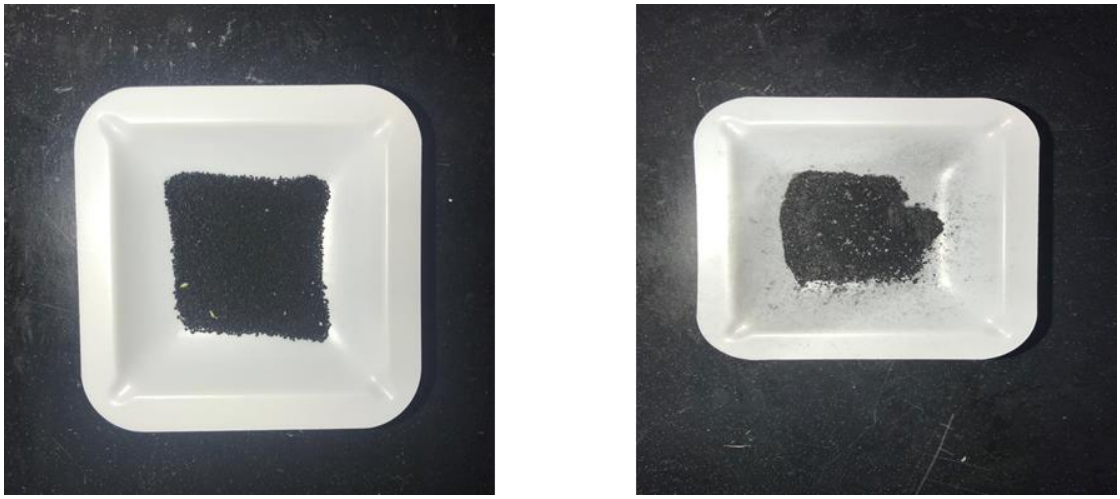

Fig. 18. Pictures of fresh $Mo_2C/\gamma\text{-}Al_2O_3$ (pelletized) (left) and spent $Mo_2C/\gamma\text{-}Al_2O_3$ (pelletized) (right).

Another preparation method called reverse microemulsion – wet impregnation method (RME-WI) was developed to synthesize $MoOx/\gamma\text{-}Al_2O_3$ and $Mo_2C/\gamma\text{-}Al_2O_3$ catalysts nanoparticles as a reference.

Molybdenum oxide supported on alumina nanoparticles was prepared via a Reverse Microemulsion – Wet Impregnation method, which is a two-emulsion method with the addition of wet impregnation method. The microemulsion systems of aluminium nitrate and ammonia solution used in this method consisted of exact same compositions and were prepared by the same method. Microemulsion III was then slowly added into the microemulsion II mixture while stirring. Following sufficient mixing, the microemulsion was allowed to settle and white particles were precipitated. After centrifugation, these particles were separated from the reverse microemulsion and washed with water and pure ethanol several times to remove remaining chemicals (the ratio of ethanol to water is 3 to 1). The resulting gel-like particles were evaporated at 100°C and calcined at 550°C for 4 hours to produce Al_2O_3. AHM dissolved in ammonia solution was added to Al_2O_3 prepared by RME method. After 30 min of sonication and 30 min of stirring, the catalyst was evaporated at 100°C and calcined at 550°C for 4

hours to produce $MoO_3/\gamma\text{-}Al_2O_3$. To synthesize $Mo_2C/\gamma\text{-}Al_2O_3$, the $MoO_3/\gamma\text{-}Al_2O_3$ was carburized in a quartz tube under the flow of H_2:CH_4 with a molar ratio of 4:1 (0.5 L/min total flow rate). The heating rate was set to 5 ℃/min from room temperature to 250℃ and 1℃/min from 150℃ to 800℃. The sample was then held at 800℃ for 2 hours under the same H_2:CH_4 flow followed by reduction in H_2 (0.5 L/min) for 1 hour followed by cooling down to room temperature under N_2 (0.5 L/min).

Table 1. The microemulsion system compositions used for the synthesis of molybdenum oxide supported on alumina nanoparticles.

	microemulsion I	**microemulsion II**	**microemulsion III**	**vol %**
aqueous phase	AHM	$Al(NO_3)_3$	NH_4OH	15
surfactant	Triton X-100	Triton X-100	Triton X-100	10
cosurfactant	2-propanol	2-propanol	2-propanol	40
oil phase	cyclohexane	cyclohexane	cyclohexane	35

4.2 Flow system setup

The flow system used for reactor testing is shown in Figure 19. The CO_2 and H_2 could be controlled by two mass flow controllers (TMCs) to feed to the reactor. The configuration of a 1/4″ stainless steel union tee (Swagelok) connected to 1/4″ stainless steel tubing (Swagelok) on both sides is the reactor used for catalytic performance evaluation, with a type K type thermocouple (1/8″, Omega Engineering, Inc.) seated inside the reactor contacting with the catalytic bed directly. After loading the catalyst through the opening tee, a plug (Swagelok) was sealed consequently. A furnace

(Thermo Fisher Scientific, Lindberg/Blue M™ Mini-Mite™ Tube Furnaces) was used for heating the reactor to provide the reaction conditions. The reactor was seated in the middle of furnace during the reaction. A furnace built-in temperature controller (UP150, Yokogawa) was used to control the temperature with the thermocouple installed within the reactor. The reactor pressure was adjusted by a back-pressure regulator (Swagelok, S01094789B). A mist trap (SMC Corporation, AFM40-N02-Z-A) and a silica gel column (Agilent Technologies, 5182-9411, the original adsorbent was replaced with orange silica gel, Fisher Scientific) were installed to remove the water from the outlet stream. Analytical instruments, such as IR analyzer (IR-208, Infrared Industries, Inc., USA) in combination with an analog-to-digital converter (USB 6008, National Instruments) and LabVIEW (National Instruments) were used to measure and record the concentrations of CH_4, CO_2 and CO continuously in the outlet stream on a dry basis.

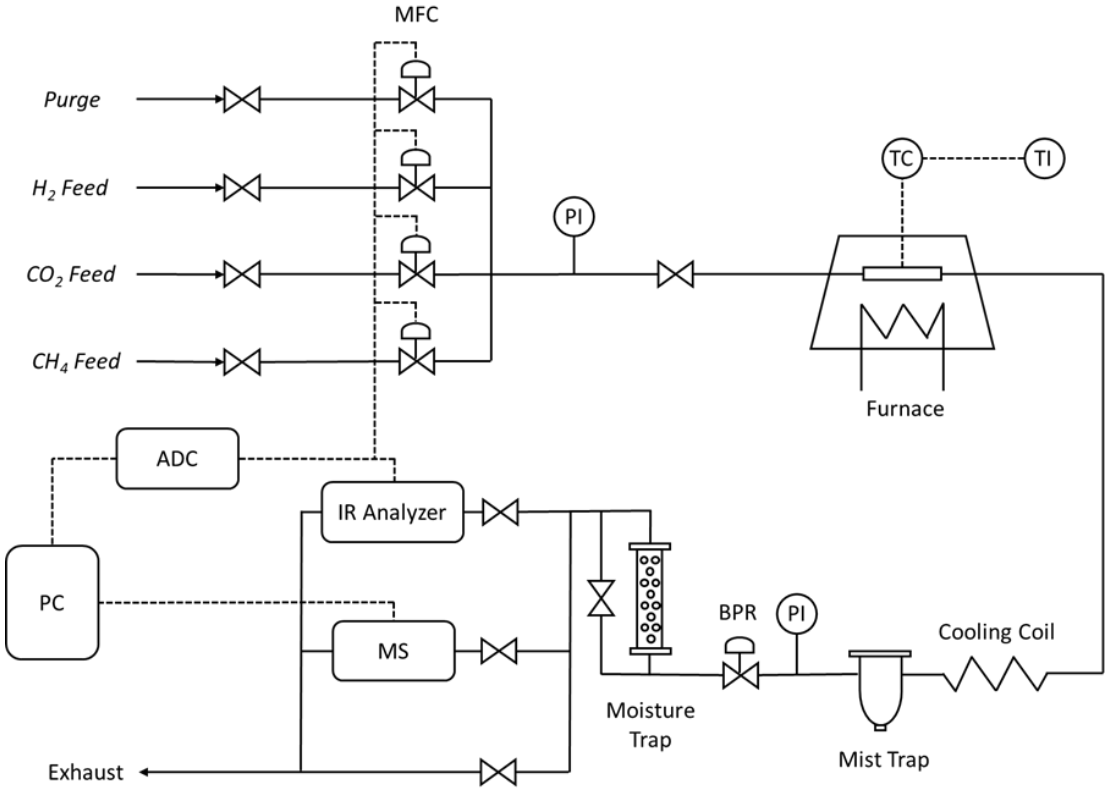

Fig. 19. Flow system setup for catalytic performance evaluation.

4.3 Catalyst characterization

Temperature programmed reduction (TPR) was performed on the fresh catalysts using the catalyst characterization instrument equipped with a thermal conductivity detector (TCD) (AMI-300Lite, Altamira Instruments) under 5 °C/min heating rate and the flow of 10% H_2/Ar mixture. Transition electron microscope (TEM) micrographs were obtained using a Zeiss microscope (100 kV). Elemental mapping results of the catalyst was obtained by scanning electron microscopy coupled to energy dispersive spectroscopy (SEM-EDS) using a Zeiss microscope (20 kV). X-ray diffraction (XRD) patterns were obtained using a D8 Discover diffractometer (Bruker). Specific surface area (SSA) was measured by a surface area analyzer (Gemini VII 2390, Micromeritics Instrument Corporation) using nitrogen as adsorption gas. Chemical composition was verified using inductively coupled plasma optical emission spectrometry (ICP-OES) (Prodigy SPEC, Leeman Labs Inc.). In order to investigate the extent of coking, thermal gravimetric analysis (TGA) (Q500, TA Instruments) was conducted on the spent catalysts. For the temperature lower that 150 °C, temperature ramp was set to 10 °C/min while over the temperature range of 150-800 °C temperature ramp was set to 2 °C/min under the air flow of 40 mL/min. TGA was in combination with the temperature programmed oxidation (TPO) under identical conditions, and the concentration of CO_2, CO and O_2 was measured at the reactor outlet using an FTIR analyzer (MultiGas™ 2030, MKS Instruments) and a mass spectrometer (MS) (HPR-20, Hiden Analytical).

4.4 Catalyst performance evaluation

The catalytic performance of the catalysts was evaluated with regard to CO_2 conversion and selectivity to CO formation at different temperatures and space velocities. The gas hourly space velocity (GHSV) is defined as follows (W_c is the

catalyst weight and Q_f is the volumetric feed flow rate):

$$GHSV = \frac{Q_f}{W_c} \tag{7}$$

Eq. (8) and Eq. (9) present the formulas of CO_2 conversion and CO selectivity respectively. As shown in equations (8)-(9), y_{CH_4}, y_{CO} and y_{CO_2} are the mole fractions of methane, carbon monoxide and carbon dioxide measured by the IR analyzer.

$$X_{CO_2} = \frac{y_{CO} + y_{CH_4}}{y_{CO_2} + y_{CO} + y_{CH_4}} \tag{8}$$

$$S_{CO} = \frac{y_{CO}}{y_{CO} + y_{CH_4}} \tag{9}$$

Carbon balance is defined as the total rate of carbon fed to the reactor divided by the rate of carbon exiting the reactor, as defined by:

$$CB = (y_{CO_2} + y_{CO} + y_{CH_4})(1 + \alpha - f_1 - 4f_2) \tag{10}$$

In Eq. (10), α, f_1 and f_2 are the ratio of H_2:CO_2 in the feed, conversion to carbon monoxide and conversion to methane, respectively. These expressions are obtained from Eqs (10a)-(10c); $F_{C,out}$ is the total outlet carbon-based molar flow rate:

$$\alpha = \frac{F_{H_2,f}}{F_{CO_2,f}} \tag{10a}$$

$$f_1 = \frac{y_{CO}}{y_{CO_2} + y_{CO} + y_{CH_4}} \equiv \frac{F_{CO,out}}{F_{C,out}} = \frac{F_{CO,out}}{F_{CO_2,f}} \tag{10b}$$

$$f_2 = \frac{y_{CH_4}}{y_{CO_2} + y_{CO} + y_{CH_4}} \equiv \frac{F_{CH_4,out}}{F_{C,out}} = \frac{F_{CH_4,out}}{F_{CO_2,f}} \tag{10c}$$

Eqs (10a)-(10c) in combination with Eq. (10e) define the total outlet molar flow rate ($F_{CH_4,out}$ and $F_{CO,out}$ are correspond to the H_2 consumption in the reverse water gas shift reaction, Eq.(1)).

$$CB = \frac{(y_{CO_2} + y_{CO} + y_{CH_4})F_{t,out}}{F_{CO_2,f}} \quad (10d)$$

$$F_{t,out} = F_{CO_2,f} + F_{H_2,f} - F_{CO_2,out} - 4F_{CH_4,out} \quad (10e)$$

Carbon balance (CB) was measured and recorded continuously in all experiments by using LabVIEW. Deviations did not exceed 5% in all experiments, in other words, the carbon balance maintained ranging 95% - 105%.

$Mo_2C/\gamma\text{-}Al_2O_3$ (RME and RME-WI) and $MoOx/\gamma\text{-}Al_2O_3$ (RME and RME-WI) were synthesized, evaluated on the flow system and characterized as discussed above.

Chapter 5

Results and Discussion

In this chapter, experimental results of the catalytic performance evaluation over various reaction conditions and stability test are shown and discussed.

5.1 Reverse water gas shift equilibrium

Because the reverse water gas shift reaction, Eq. (1), is reversible, the maximum conversion will be limited by equilibrium and will be a function of temperature. The equilibrium conversion can be evaluated analytically [27]. By first defining the total conversion and H_2/CO_2 feed ratio as in Eq. (11), expressions for the extent of each species at equilibrium can be derived (assuming no CH_4 formation), Eq. (12).

$$f_1 = \frac{n_{CO_2,f} - n_{CO_2,eq}}{n_{CO_2,f}}$$
$$\alpha = \frac{n_{H_2,f}}{n_{CO_2,f}} \tag{11}$$

$$\phi_{CO_2} = 1 - f_1$$
$$\phi_{H_2} = \alpha - f_1$$
$$\phi_{CO} = f_1$$
$$\phi_{H_2O} = f_1 \tag{12}$$

Equilibrium partial pressures can then be estimated using the equilibrium extents derived above, i.e.

$$P_i = y_i P = \left(\frac{\phi_i}{\sum \phi_j} \right) P$$

$$P_{CO_2} = \frac{1 - f_1}{1 + \alpha} P$$

$$P_{H_2} = \frac{\alpha - f_1}{1 + \alpha} P \tag{13}$$

$$P_{CO} = \frac{f_1}{1 + \alpha} P$$

$$P_{H_2O} = \frac{f_1}{1 + \alpha} P$$

where y_i and P are mole fraction and total pressure, respectively.

These equilibrium partial pressures can then be substituted into the reverse water gas shift equilibrium constant:

$$K_{RWGS} = A_{RWGS} \exp\left(\frac{-\Delta H^{\circ}_{RWGS}}{R_g T}\right) = \frac{P_{CO} P_{H_2O}}{P_{CO_2} P_{H_2}} = \frac{f_1^2}{(1 - f_1)(\alpha - f_1)} \tag{14}$$

The final equation to be solved is given as follows:

$$A_{RWGS} \exp\left(\frac{-\Delta H^{\circ}_{RWGS}}{R_g T}\right) = \frac{f_1^2}{(1 - f_1)(\alpha - f_1)} \tag{15}$$

Note that the equilibrium conversion will be dependent on temperature as well as H_2/CO_2 feed ratio, but will not depend on pressure, since there is no change in number of moles, Eq. (1).

5.2 Comparison between supported Mo_2C and MoOx

The Mo-catalysts were synthesized and evaluated in terms of CO_2 conversion and selectivity to CO as a function of temperature and GHSV. Conversion profiles for all catalysts showed similar trends over the 300 to 600°C temperature range with a constant space velocity of 60,000 ml/(g h) as shown in figure 20. As expected,

conversion increased linearly with temperature and near equilibrium conversions were achieved for temperatures higher than 450°C. All catalysts showed complete selectivity to CO over the entire temperature range.

Performance of all catalysts were also compared at varying GHSVs as shown in figure 21. As expected, conversion decreased with increasing GHSV due to shorter contact times. The CO_2 conversion maintained ranging 55-59% for Mo_2C (RME) and Mo_2C (RME-WI) at varying GHSVs. The highest conversion achieved was 59% for both Mo_2C (RME) and Mo_2C (RME-WI) which was approximately the equilibrium conversion. Derivations of CO_2 conversion for MoOx (RME) and MoOx (RME-WI) were observed from the results shown in Figure 20 under the similar reaction conditions. CO_2 conversion of MoOx (RME) dropped from 52% to 38% due to deactivation. The selectivity of all catalysts towards CO formation was complete at all GHSVs.

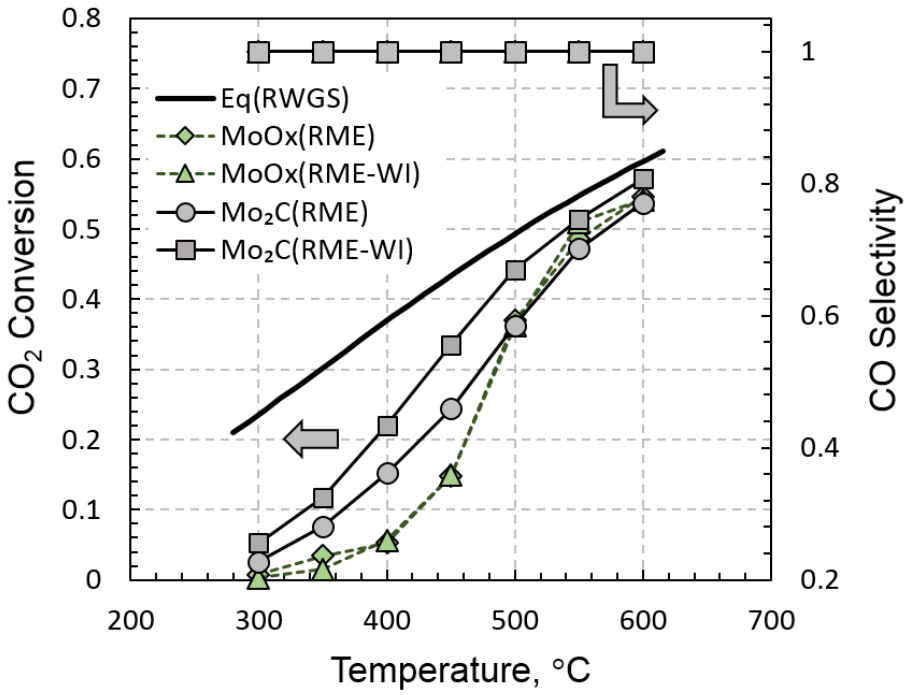

Fig. 20. Catalytic performance of supported MoOx and Mo_2C catalysts synthesized by different methods at varying temperatures. GHSV=60,000 ml/ (g h), P=3 bar, H_2: CO_2=3.

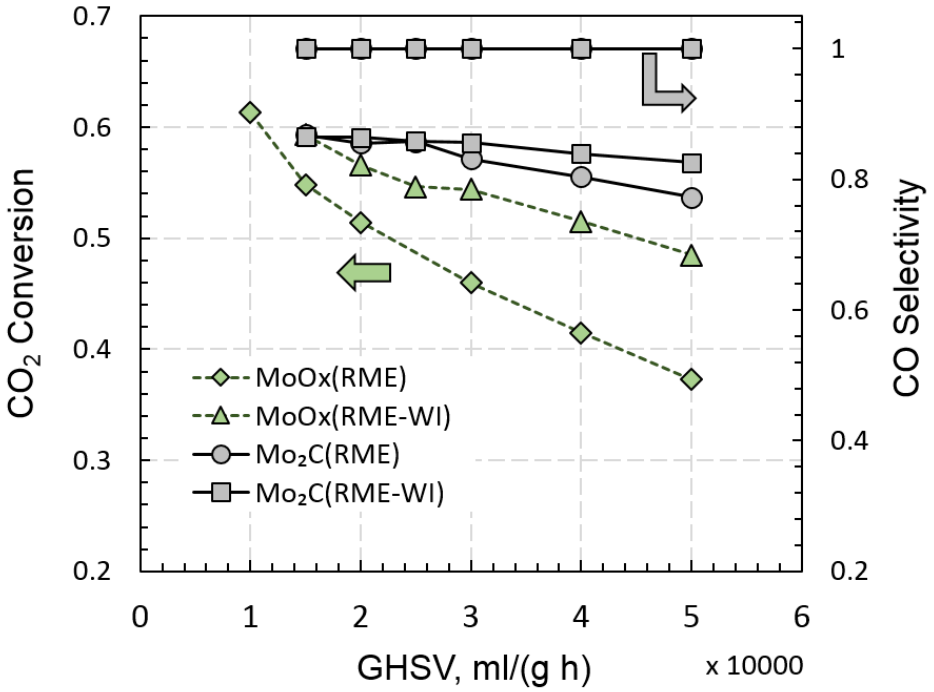

Fig. 21. Catalytic performance of supported MoOx and Mo_2C catalysts synthesized by different methods at varying temperatures and GHSV. Temperature = 600°C, P=3 bar, H_2: CO_2=3.

5.3 Stability evaluation

Catalysts are often deactivated due to coking and sintering when operated at elevated temperatures and common industrial operating conditions, i.e., high GHSV and high pressure. Catalyst stability is an important parameter for performance, often overlooked in laboratory studies. Stability tests were conducted for the Mo-catalysts (RME and RME-WI) as shown in Figure 22. Results indicated that all catalysts successfully maintained complete selectivity to CO with no CH_4 formation through over 100 hours on stream. Mo_2C (RME) catalyst showed relative stability, achieving CO_2 conversion of 60% at the beginning of operation with no obvious decline over the full time on stream. With the MoOx (RME) catalyst, initial conversion was observed around 48%, increased to 56% after 32h on stream and remained at this value for the remainder of time on stream. Catalysts synthesized by RME-WI method showed nearly identical performance with an initial conversion of 50%, rising to 56% after 60 h on

stream, followed by a slight drift for the remainder of time on stream. A comparison of the stability test results indicates that Mo_2C (RME) exhibits the highest stability as a CO_2 hydrogenation catalyst when tested over 100 h on stream.

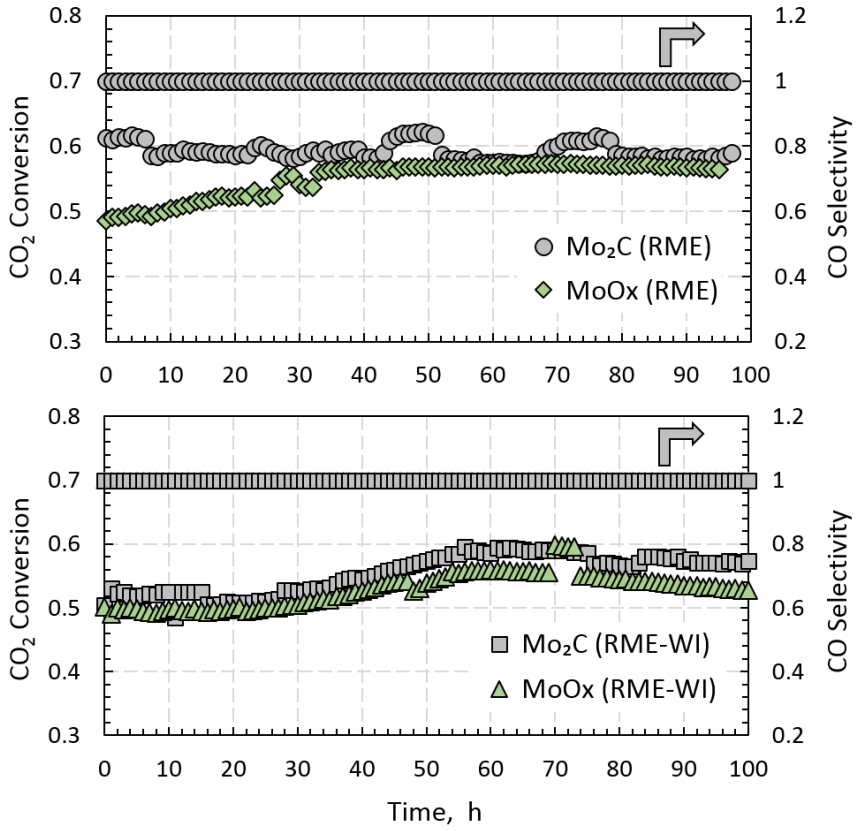

Fig. 22. Stability tests on supported MoOx and Mo_2C catalysts. Temperature = 600°C, GHSV=60,000 ml/ (g h), P=3 bar, H_2: CO_2=3.

Thermal gravimetric analysis (TGA) combined with temperature programmed oxidation (TPO) was performed on spent Mo-catalysts after 100 h on stream shown in Figure 23. All samples displayed initial weight decrease of approximately 1% at T < 250°C which is associated with the water desorption from the sample.

For MoOx (RME), over the 260 – 450°C temperature range, the sample weight increased by ca. 4% and then decreased by ca. 20% over 450 – 650°C temperature range. Beyond 260°C the catalyst had a weight increase due to the oxidation of MoO_2/γ-Al_2O_3 formed on the surface during the reaction back to MoO_3/γ-Al_2O_3. After that the weight

loss is attributed to deposited carbon oxidation as is evident from CO_2 and CO signals detected by the FTIR. A gradual decline begins at ca. 450° C with a sharp peak at 550 °C, which is clearly associated with the sharp peaks of CO_2 and CO release. Compared with MoOx (RME), MoOx (RME-WI) showed a similar weight loss trend but with a smaller weight loss percentage. For MoOx (RME-WI), the sample weight increased by ca. 4% from 200°C to 500°C and then decrease by ca. 2% over the 500 - 650°C temperature range, where the weight gained is due to the oxidation of MoO_2/γ-Al_2O_3 to MoO_3/γ-Al_2O_3 where the weight loss is attributed to the deposited carbon oxidation confirmed by the peaks of CO_2 and CO released at the same temperature (550°C). The FTIR signals for the MoOx(RME) appear lower compared to the signals detected from MoOx(RME), which is consistent with the percentage of weight loss associated with each catalyst.

For Mo_2C (RME), over the 200 – 400°C temperature range, the sample weight increased by ca. 2% and then decreased by a similar amount over the 400 – 550°C temperature range. The weight loss is attributed to deposited carbon oxidation as it is evident from the CO_2 and CO signals detected by FTIR. The gradual decline begins at ca. 400° C with a sharp peak at 450 °C, which is clearly associated with the sharp peaks of CO_2 and CO release. As for Mo_2C (RME-WI), there is an obvious secondary peak of CO_2 which occurred along with a mild increase in sample weight over the temperature range from 200 to 380°C. This could be associated with the surface oxidation of the sample from Mo_2C to MoOx, with the bulk of the catalyst remaining as a carbide. The weight increase can be associated with the oxidation of Mo_2C and MoOx as the catalyst is expected to be reduced to a certain extent under the reaction conditions due to the presence of excess H_2. Surface oxidation of the sample includes conversion of MoO_3 to MoO_2 and Mo_2C to MoOx.

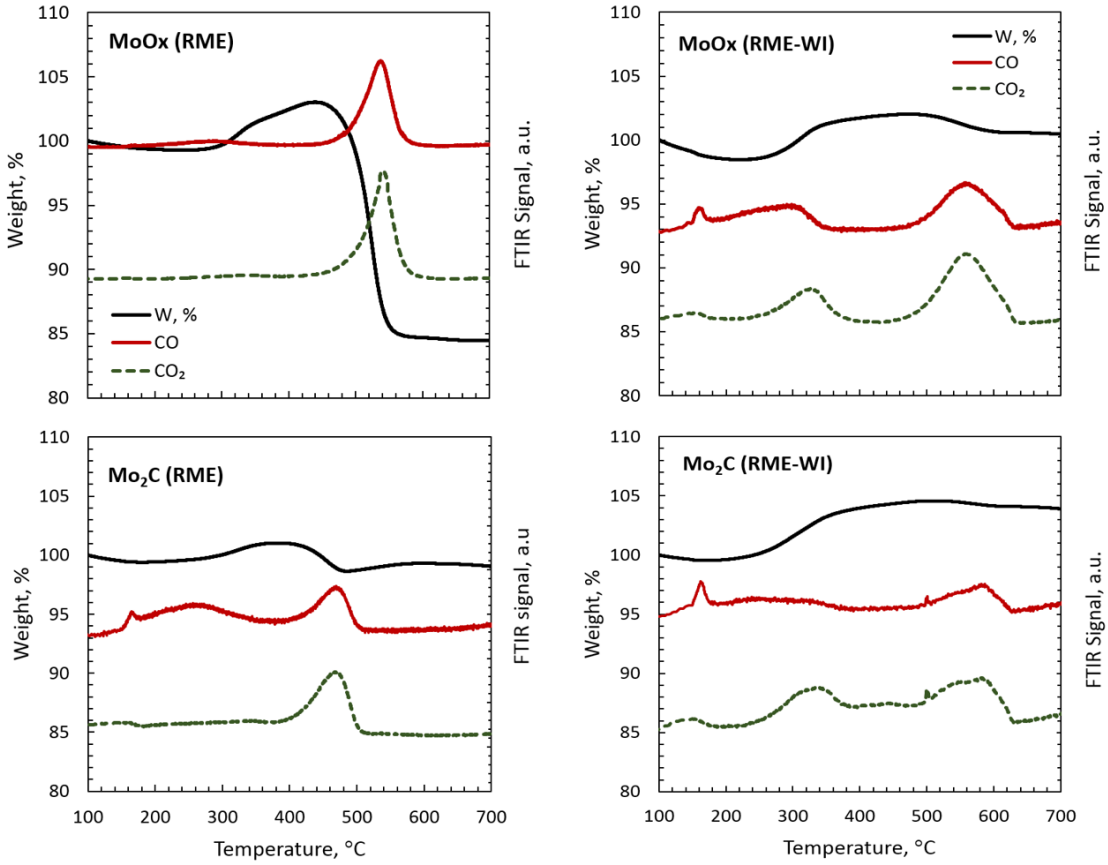

Fig. 23. TGA-FTIR results for MoOx/γ-Al_2O_3 and Mo_2C/γ-Al_2O_3 synthesized by RME and RME-WI methods after 100 h stability test at 800°C, temperature ramping rate of 10°C/min for temperature ≤ 150°C and 2°C/min for temperature between 150 and 800°C.

The TGA results are consistent with the stability test. The deposited carbon on the surface of Mo_2C/γ-Al_2O_3(RME) are seen to be the least extent and oxidized at lower temperature, which could explain the generally better stability with no obvious coking and deactivation process of this catalyst.

Chapter 6

Characterization Results

In this chapter, catalyst characterization conducted by ICP-MS, SEM-EDS, TPR, TEM, XRD and some other catalyst characterization results are presented. These results were analyzed leading to the discussion on reaction mechanisms, including activity, selectivity, and stability.

6.1 Molybdenum-based catalysts

Gas profiles taken over the course of carburization for MoOx catalysts prepared via both RME and RME-WI methods are compared in Figure 24. Profiles for both catalysts appear to have similar features. One notable difference is that the main CO peak which occurs at 650°C and the smaller CO_2 peak which occurs at 680°C for MoOx catalyst synthesized by RME method. Alternatively, the MoOx catalyst synthesized by RME-WI method shows both CO and CO_2 peaks occurs at approximately 600°C.

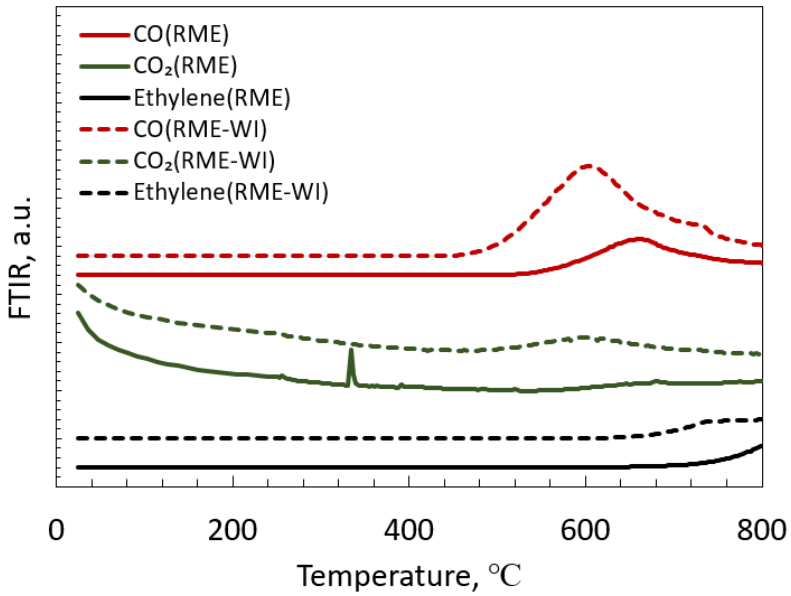

Fig. 24. Gases profile for CO_2, CO and C_2H_4 during carburization of MoOx (RME) and MoOx (RME-WI) catalysts.

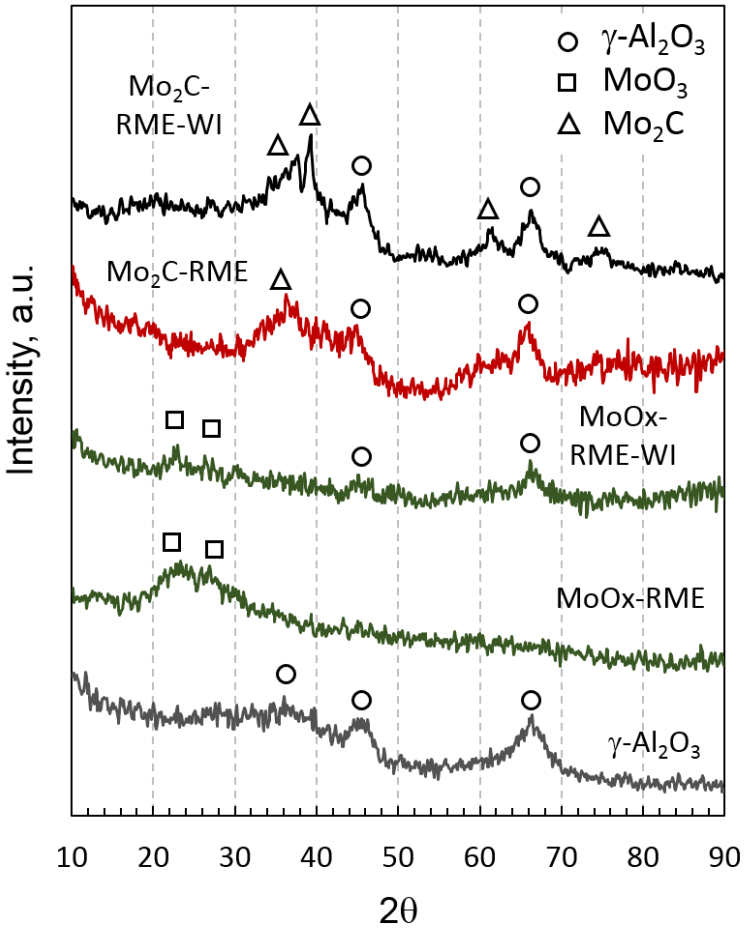

Fig. 25. XRD patterns of fresh supported molybdenum catalysts and γ-Al_2O_3.

In order to better understand the structure, morphology and reaction mechanisms of the catalysts, XRD, SEM-EDS and TEM studies were performed.

Figure 25 shows the XRD patterns for alumina synthesized via RME and other fresh supported Mo-based catalysts synthesized through RME and RME-WI methods. As expected, the characteristic peaks of MoO_3 were identified for both MoOx catalysts at $2\theta = 23.3$ and 27.3°. Similar results were obtained for both Mo_2C catalyst with Mo_2C peaks showing at $2\theta = 34.4°$ for Mo_2C (RME) and $2\theta = 38.0°$, 61.5° for Mo_2C (RME-WI). Characteristic peaks of Al_2O_3 were observed in all fresh catalyst except MoOx (RME) due to weak crystallization. Catalysts synthesized by RME showed better dispersion of small MoOx clusters on the Al_2O_3 surface.

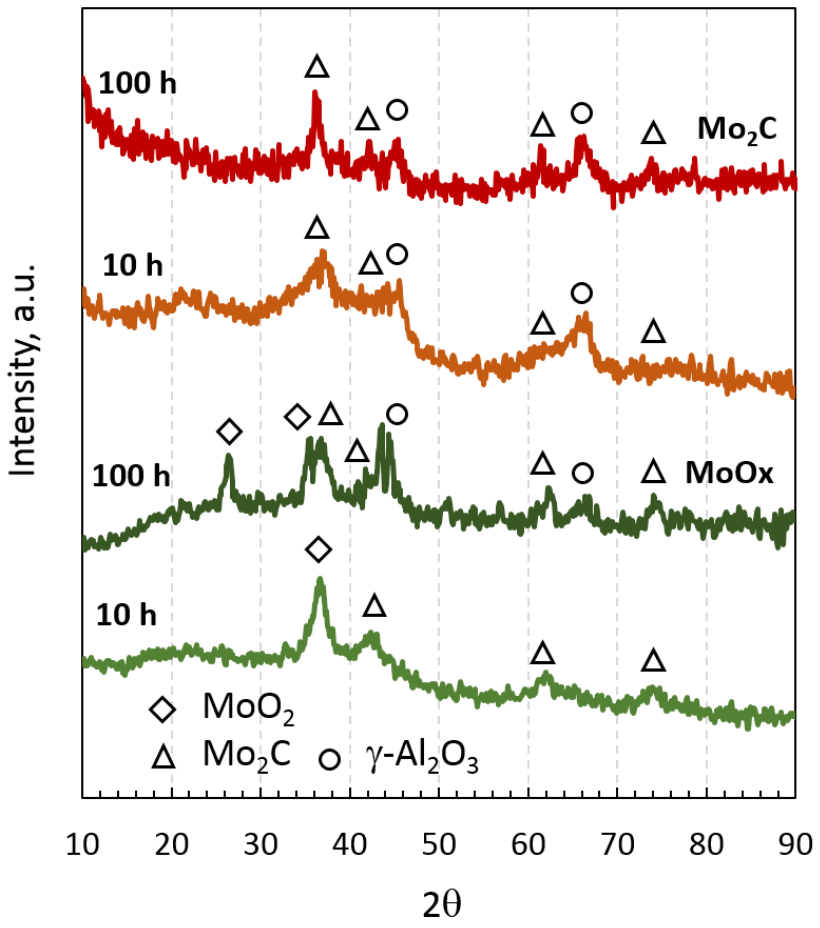

Fig. 26. XRD patterns of spent supported molybdenum catalysts synthesize by RME method.

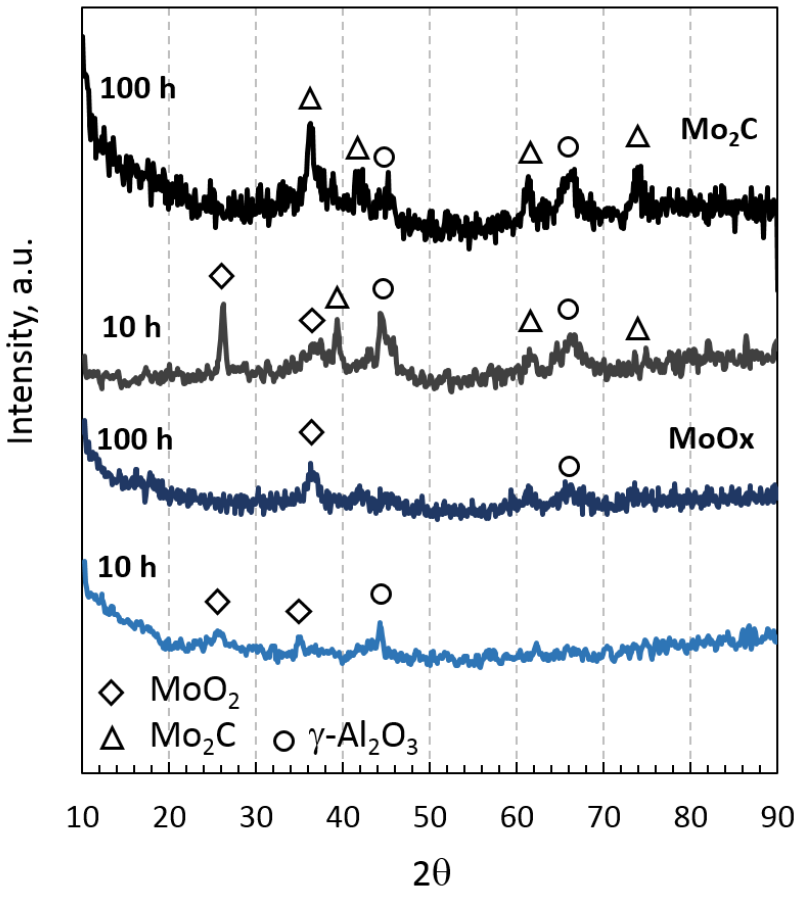

Fig. 27. XRD patterns of spent supported molybdenum catalysts synthesized by RME-WI method.

XRD patterns of spent catalysts are shown in Figures 26 and 27. The MoOx (RME and RME-WI) after reaction seems to undergo reduction to form MoO_2 with associated peaks identified at 2θ=37.0° and 2θ = 26.1°, 37.0°, respectively. The spent MoOx (RME) also shows additional peaks of Mo_2C at 2θ = 43.8°, 63.0° and 74.0°. The sharp peaks associated MoO_2 and Mo_2C were clearly observed for MoOx (RME) after the stability test, which may explain the large amounts of carbonate reported by the TGA-FTIR and is consistent with TPR result. No Mo_2C peaks were recognizable in the MoOx (RME-WI) after stability test. The characteristic peaks of Mo_2C were identified for both Mo_2C catalysts. The spent Mo_2C (RME-WI) shows additional peaks of MoO_2 at 2θ =26.1° and 37.0°. Similar results were obtained for both Mo_2C catalyst after the

stability test with Mo_2C peaks showing at 2θ = 36.0°, 43.6°, 63.4° and 75.5°. Mo_2C (RME) were relatively more stable after reaction at high temperature.

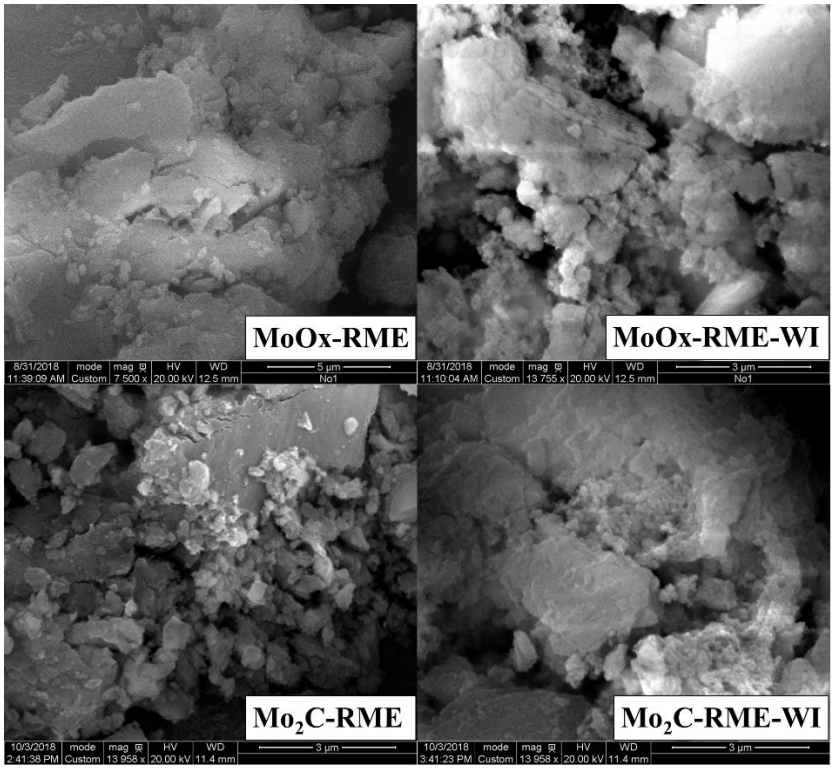

Fig. 28. SEM micrographs of fresh supported catalysts synthesized via RME and RME-WI methods.

To analyze particle dispersion on the support material, SEM micrographs were prepared for all fresh samples as shown in Figure 28. The micro-scale morphology of catalysts synthesized by different methods show large similarities. Molybdenum is well-dispersed throughout all sample confirming homogeneity of the catalytic surface. Additionally, Molybdenum interacts well with the support material in the catalysts synthesized by the RME method.

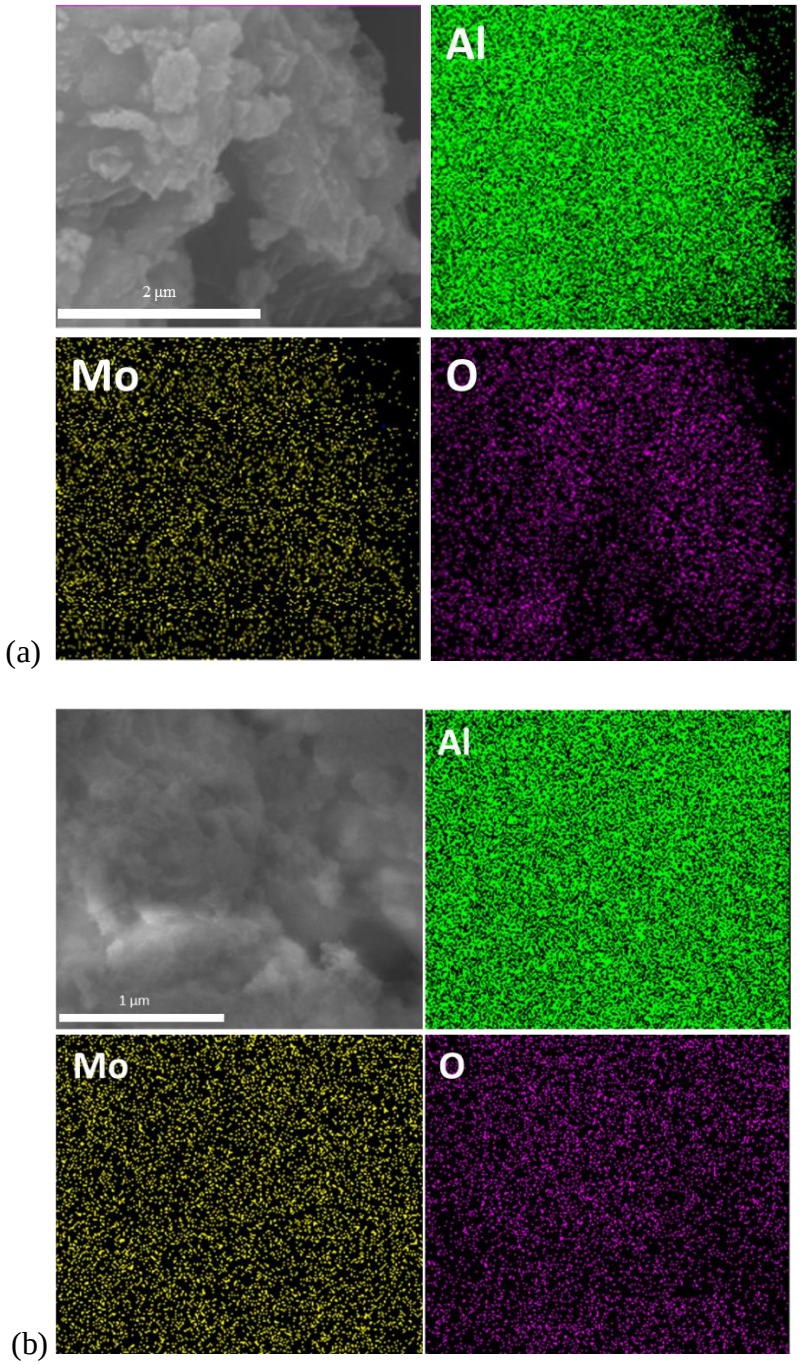

Fig. 29. SEM-EDS analysis of (a) Mo_2C (RME) and (b) Mo_2C (RME-WI).

To analyze the dispersion of active phases in the catalysts, SEM-EDS elemental mappings of the Mo_2C (RME) and Mo_2C (RME-WI) catalysts were performed, as shown in Figure 29. The mapping showed generally good dispersion of all elements. Remarkably, Mo is well-dispersed throughout the sample. These findings are consistent with the catalytic performance evaluation and XRD analysis.

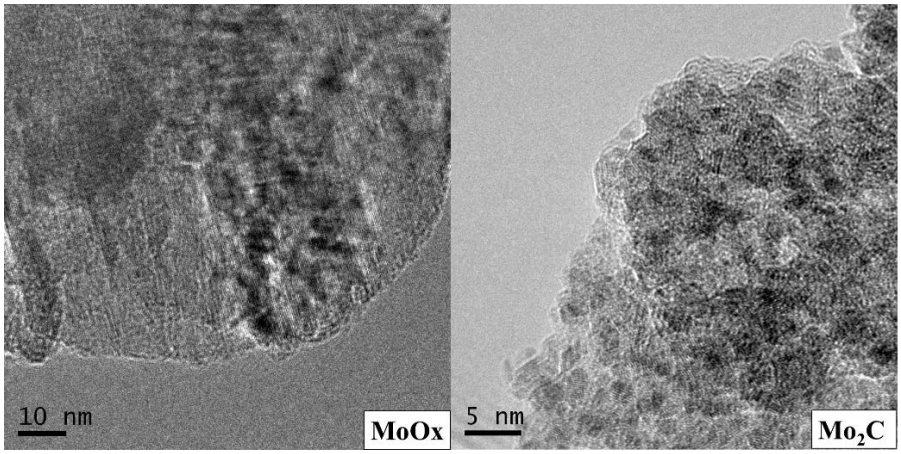

Fig. 30. TEM images of spent supported catalysts synthesized by RME method.

TEM images of the spent catalysts (tested at 600 °C at a GHSV of 60,000 ml $h^{-1} g_{cat}^{-1}$, pressure = 3 bar, and H_2:CO_2= 3 for over 100 h on stream) are shown in Figure 30. A similar round-shaped morphology was observed for both MoOx and Mo_2C nanoparticles with particle sizes ranging from 1-5 nm. These values are consistent with calculated crystallite sizes (as shown in Table 2).

Fresh catalysts compositions were verified using ICP-OES. The compositions did not vary significantly from the target values of 20 wt.% (as shown in Table 2). BET surface area was measured for all catalysts with results summarized in Table 2. Catalysts synthesized by the RME method show a higher surface area than catalysts synthesized from the RME-WI method. Crystallite sizes were calculated by Scherrer equation and are shown in Table 2. Catalysts synthesized via the RME method show smaller crystalline sizes as compared to the catalysts synthesized via the RME-WI method.

Table 2. Characteristic of the fresh supported molybdenum catalysts synthesize by different methods.

Sample	Mo loading (wt %)	surface area (m^2/g)	crystallite size (nm)
MoOx(RME)	16.9	380.0	2.1
MoOx(RME-WI)	20.4	263.8	16.7
Mo_2C(RME)	17.8	191.2	1.8
Mo_2C(RME-WI)	24.9	179.5	12.4

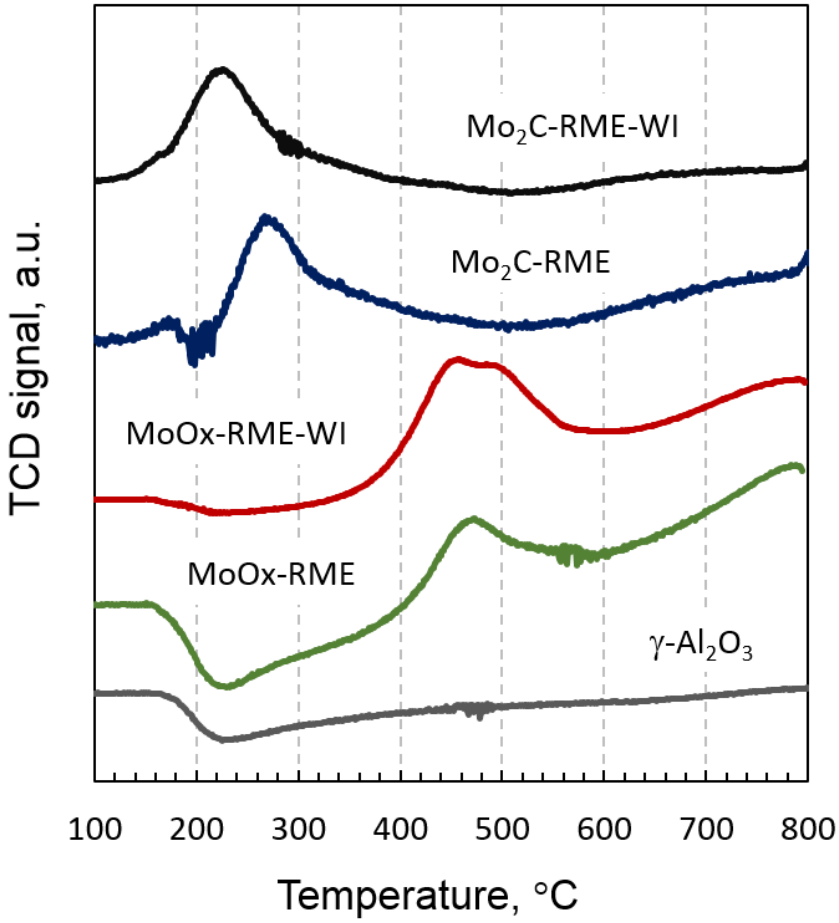

Fig. 31. Temperature programmed reduction of γ-Al_2O_3 (RME) and fresh supported Molybdenum catalysts synthesized by RME and RME-WI methods.

To investigate the mechanism responsible for enhanced catalytic activity, all fresh catalysts were analyzed by temperature programmed reduction (TPR). H_2 consumption for each fresh Mo based catalysts are shown in Figure 31. A similar peak

location is observed for catalysts despite differing synthesis methods. Typical H_2 consumption peaks centered at ~ 480℃ are associated with the $MoO_3 \rightarrow MoO_2$ transition and are present in both fresh MoOx catalysts. An additional gradual increase starts at ca. 580 ℃ with a peak at 790 ℃ clearly associated with H_2 consumption for MoOx(RME). Alternatively, peaks of the Mo_2C catalyst result as their surfaces are covered with carbon atoms following carburization, which are reduced to CH_4 in the 250 - 300℃ temperature range.

Chapter 7

Conclusions and Future Work

In this chapter, conclusions on this study and future work related to the project are discussed.

7.1 Reverse water gas shift reaction over Mo-based catalysts synthesized by reverse microemulsion method

The high surface area Mo-based nanoparticles have been successfully achieved through reverse microemulsion method which were confirmed by the ICP-OES, BET SAA, XRD, SEM and TEM techniques. The BET SAA indicated that the surface area of MoOx(RME), Mo_2C(RME), MoOx(RME-WI) and Mo_2C(RME-WI) are 380.0, 263.8, 191.2 and 179.5 m^2/g respectively, which are significantly high. TPR result reveals the reducibility of MoOx(RME), Mo_2C(RME), MoOx(RME-WI) and Mo_2C(RME-WI). Both of MoO_3 catalysts synthesized by RME and RME-WI method were reduced to MoO_2 at very similar temperature. The reduction peak of Mo_2C (RME-WI) appeared at lower temperature than Mo_2C(RME) with similar H_2 consumption. RWGS reaction over Mo-based catalysts was investigated. Mo_2C/γ-Al_2O_3 and MoOx/γ-Al_2O_3 synthesized by RME and RME-WI methods were found to exhibit excellent activity while maintaining complete selectivity to CO production in all measurements.

MoOx/γ-Al_2O_3 and Mo_2C/γ-Al_2O_3 synthesized by RME and RME-WI methods were evaluated in terms of CO_2 conversion and CO selectivity as a function of temperature and space velocity. Under the conditions tested, the catalyst was exclusively selective to CO production, attaining CO_2 conversions as high as 59% at 600°C and GHSV = 60,000 mL/(g h). No significant deactivation was observed over 100 hours on stream. Catalytic performance results present that Mo_2C/γ-Al_2O_3

synthesized by RME and RME-WI methods have better CO_2 conversion than MoOx/γ-Al_2O_3 synthesized by RME and RME-WI over the range of 300-450 ℃. MoOx/γ-Al_2O_3 and Mo_2C/γ-Al_2O_3 synthesized by RME and RME-WI methods provide outstanding catalytic performance approaching equilibrium over the range of 450-600℃. Mo_2C (RME-WI) was exhibited the best activity over all temperatures at GHSV = 60,000 mL/(g h), P = 3 bar and H_2:CO_2 =3:1.

Apparent CO_2 conversion improvements were achieved for Mo_2C/γ-Al_2O_3 synthesized by RME and RME-WI methods over the GHSV range of 15,000 – 50,000 mL/(g h) as compared with MoOx/γ-Al_2O_3 (RME and RME-WI). Mo_2C (RME-WI) was found to possess the best activity over all GHSVs as well. The catalytic formulation was successfully developed, allowing for high production rates, completely selective to CO formation and withstanding high temperatures being stable with respect to sintering and coking.

7.2 Future work

Future work is required on both reactor design and experimental investigations.

After developing the Mo_2C/γ-Al_2O_3 catalyst synthesized by novel preparation method and improving the catalytic performance experimentally, a rate equation is required to be determined for the catalyst. This rate equation could be used to predict catalytic performance over a wide range of operating conditions and assess the potential practical applications. Therefore, the mechanism of RWGS reaction occurring on the Mo_2C/γ-Al_2O_3 catalyst still need to be verified and requires investigation.

A H_2-permable tubular membrane reactor would be developed, which integrated the dual reactions for converting CO_2 and CH_4 into synthetic valuable products, i.e., syngas (H_2 and CO) and C_2 (ethylene and acetylene). The reactor consists of a selective

permeation membrane (i.e. ceramic membrane) supported on a porous tube which allowing H_2 separation [66]. In the inner membrane compartment, non-oxidative methane conversion (NMC) could occur to produce C_{2+} and H2 over a Fe-based catalyst [67]. Outside the membrane, H_2 permeated from inner membrane compartment could react with CO_2 as a sweep gas to generate syngas by the reverse water gas shift (RWGS) reaction. The reduction of greenhouse gas (CH_4 and CO_2) could be achieved simultaneously with the generation of synthetic valuable products.

Regarding the experimental investigation, the difference between RME and RME-WI method is required to be investigated and the improvement on reverse microemulsion method needs to be studied. For industrial applications, significantly higher space velocities and pressures may be required, so the catalysts need to be evaluated under the industrially relevant conditions experimentally which could be compared with modelling results as described above. Furthermore, the effect of different loadings of Mo and promotion of another metal should also be done which may improve the catalytic performance possibly.

References

[1] World Energy Outlook 2017, International Energy Agency, 2017.
[2] J. Hansen, M. Sato, R. Ruedy, K. Lo, D.W. Lea, M. Medina-Elizade, Global temperature change, P Natl Acad Sci USA 103 (2006) 14288-14293.
[3] G.T.J.S. Rochelle, Amine scrubbing for CO2 capture, 325 (2009) 1652-1654.
[4] Y. Yuan, H. You, L.J.C.J.o.C.E. Ricardez-Sandoval, Recent advances on first-principles modeling for the design of materials in CO2 capture technologies, (2018).
[5] T. Nittaya, P.L. Douglas, E. Croiset, L.A.J.F. Ricardez-Sandoval, Dynamic modelling and control of MEA absorption processes for CO2 capture from power plants, 116 (2014) 672-691.
[6] A. Chansomwong, K. Zanganeh, A. Shafeen, P. Douglas, E. Croiset, L.J.I.J.o.G.G.C. Ricardez-Sandoval, Dynamic modelling of a CO2 capture and purification unit for an oxy-coal-fired power plant, 22 (2014) 111-122.
[7] Z. He, L.A.J.I.J.o.G.G.C. Ricardez-Sandoval, Dynamic modelling of a commercial-scale CO2 capture plant integrated with a natural gas combined cycle (NGCC) power plant, 55 (2016) 23-35.
[8] M. Lucio, L.J.I.-P. Ricardez-Sandoval, Dynamic Optimization Applied for Modelling and Optimal Control of a Packed Bed Reactor for Chemical-Looping Combustion, 52 (2019) 850-855.
[9] M.D. Porosoff, B.H. Yan, J.G.G. Chen, Catalytic reduction of CO_2 by H_2 for synthesis of CO, methanol and hydrocarbons: challenges and opportunities, Energy Environ. Sci. 9 (2016) 62-73.
[10] G. Centi, S.J.C.T. Perathoner, Opportunities and prospects in the chemical recycling of carbon dioxide to fuels, 148 (2009) 191-205.
[11] W. Wang, S. Wang, X. Ma, J. Gong, Recent advances in catalytic hydrogenation of carbon dioxide, Chem. Soc. Rev. 40 (2011) 3703-3727.
[12] S. Perathoner, G.J.C. Centi, CO2 recycling: a key strategy to introduce green energy in the chemical production chain, 7 (2014) 1274-1282.
[13] D. Sun, F.M. Khan, D.S.A. Simakov, Heat removal and catalyst deactivation in a Sabatier reactor for chemical fixation of CO2: Simulation-based analysis, Chem Eng J 329 (2017) 165-177.
[14] B. Kumar, M. Llorente, J. Froehlich, T. Dang, A. Sathrum, C.P.J.A.r.o.p.c. Kubiak, Photochemical and photoelectrochemical reduction of CO2, 63 (2012) 541-569.
[15] Y. Chen, N.S. Lewis, C.J.E. Xiang, E. Science, Operational constraints and strategies for systems to effect the sustainable, solar-driven reduction of atmospheric CO 2, 8 (2015) 3663-3674.
[16] B. Ren, J. Li, G. Wen, L. Ricardez− Sandoval, E.J.T.J.o.P.C.C. Croiset, First-Principles Based Microkinetic Modeling of CO2 Reduction at the Ni/SDC Cathode of a Solid Oxide Electrolysis Cell, 122 (2018) 21151-21161.
[17] Y.A. Daza, J.N.J.R.A. Kuhn, CO 2 conversion by reverse water gas shift catalysis: comparison of catalysts, mechanisms and their consequences for CO 2 conversion to liquid fuels, 6 (2016) 49675-49691.
[18] A. Rafiee, K.R. Khalilpour, D. Milani, M.J.J.o.e.c.e. Panahi, Trends in CO2 conversion and utilization: a review from process systems perspective, (2018).
[19] E.W. Team, ESRL Global Monitoring Division - Global Greenhouse Gas Reference Network.
[20] V.G. Gude, Green chemistry for sustainable biofuel production, CRC Press2018.

[21] National Inventory Report 1990-2016: Greenhouse Gas Sources and Sinks in Canada: Executive Summary, Canada. Environment and Climate Change Canada.
[22] Electricity facts, Natural Resouces Canada.
[23] D.S.A. Simakov, Renewable Synthetic Fuels and Chemicals from Carbon Dioxide: Fundamentals, Catalysis, Design Considerations and Technological Challenges, Springer International Publishing2017.
[24] S. Hernández, M.A. Farkhondehfal, F. Sastre, M. Makkee, G. Saracco, N.J.G.C. Russo, Syngas production from electrochemical reduction of CO 2: current status and prospective implementation, 19 (2017) 2326-2346.
[25] D.S. Mallapragada, N.R. Singh, V. Curteanu, R.J.I. Agrawal, E.C. Research, Sun-to-fuel assessment of routes for fixing CO2 as liquid fuel, 52 (2013) 5136-5144.
[26] K. Oshima, T. Shinagawa, Y. Nogami, R. Manabe, S. Ogo, Y.J.C.T. Sekine, Low temperature catalytic reverse water gas shift reaction assisted by an electric field, 232 (2014) 27-32.
[27] D.S. Simakov, M.M. Wright, S. Ahmed, E.M. Mokheimer, Y.J.C.S. Román-Leshkov, Technology, Solar thermal catalytic reforming of natural gas: a review on chemistry, catalysis and system design, 5 (2015) 1991-2016.
[28] X. Chen, X. Su, H. Duan, B. Liang, Y. Huang, T.J.C.T. Zhang, Catalytic performance of the Pt/TiO2 catalysts in reverse water gas shift reaction: Controlled product selectivity and a mechanism study, 281 (2017) 312-318.
[29] A. Goguet, F. Meunier, J. Breen, R. Burch, M. Petch, A.F.J.J.o.C. Ghenciu, Study of the origin of the deactivation of a Pt/CeO2 catalyst during reverse water gas shift (RWGS) reaction, 226 (2004) 382-392.
[30] C.-S. Chen, W.-H. Cheng, S.-S.J.C.l. Lin, Mechanism of CO formation in reverse water–gas shift reaction over Cu/Al 2 O 3 catalyst, 68 (2000) 45-48.
[31] C.-S. Chen, W.-H. Cheng, S.-S.J.A.C.A.G. Lin, Study of reverse water gas shift reaction by TPD, TPR and CO2 hydrogenation over potassium-promoted Cu/SiO2 catalyst, 238 (2003) 55-67.
[32] J.A. Rodriguez, J. Evans, L. Feria, A.B. Vidal, P. Liu, K. Nakamura, F.J.J.o.c. Illas, CO2 hydrogenation on Au/TiC, Cu/TiC, and Ni/TiC catalysts: Production of CO, methanol, and methane, 307 (2013) 162-169.
[33] S.-I. Fujita, M. Usui, N.J.J.o.C. Takezawa, Mechanism of the reverse water gas shift reaction over Cu/ZnO catalyst, 134 (1992) 220-225.
[34] Y. Zhuang, R. Currie, K.B. McAuley, D.S.J.A.C.A.G. Simakov, Highly-selective CO2 conversion via reverse water gas shift reaction over the 0.5 wt% Ru-promoted Cu/ZnO/Al2O3 catalyst, 575 (2019) 74-86.
[35] C. Liu, T.R. Cundari, A.K.J.T.J.o.P.C.C. Wilson, CO2 reduction on transition metal (Fe, Co, Ni, and Cu) surfaces: In comparison with homogeneous catalysis, 116 (2012) 5681-5688.
[36] S.-G. Wang, X.-Y. Liao, D.-B. Cao, C.-F. Huo, Y.-W. Li, J. Wang, H.J.T.J.o.P.C.C. Jiao, Factors controlling the interaction of CO2 with transition metal surfaces, 111 (2007) 16934-16940.
[37] T. Bligaard, J.K. Nørskov, S. Dahl, J. Matthiesen, C.H. Christensen, J.J.J.o.C. Sehested, The Brønsted–Evans–Polanyi relation and the volcano curve in heterogeneous catalysis, 224 (2004) 206-217.
[38] C.-S. Chen, W.-H. Cheng, S.-S.J.A.C.A.G. Lin, Study of iron-promoted Cu/SiO2 catalyst on high temperature reverse water gas shift reaction, 257 (2004) 97-106.
[39] D.S. Simakov, H.Y. Luo, Y.J.A.C.B.E. Román-Leshkov, Ultra-low loading Ru/γ-Al2O3: a highly active and stable catalyst for low temperature solar thermal reforming of methane, 168 (2015) 540-549.

[40] I. del Rosal, M. Mercy, I.C. Gerber, R.J.A.n. Poteau, Ligand-field theory-based analysis of the adsorption properties of ruthenium nanoparticles, 7 (2013) 9823-9835.
[41] A.M. Karim, V. Prasad, G. Mpourmpakis, W.W. Lonergan, A.I. Frenkel, J.G. Chen, D.G.J.J.o.t.A.C.S. Vlachos, Correlating particle size and shape of supported Ru/γ-Al2O3 catalysts with NH3 decomposition activity, 131 (2009) 12230-12239.
[42] J. Gavnholt, J.J.P.R.B. Schiøtz, Structure and reactivity of ruthenium nanoparticles, 77 (2008) 035404.
[43] P. Liu, J.A.J.T.J.o.P.C.B. Rodriguez, Water-gas-shift reaction on molybdenum carbide surfaces: essential role of the oxycarbide, 110 (2006) 19418-19425.
[44] N.M. Schweitzer, J.A. Schaidle, O.K. Ezekoye, X. Pan, S. Linic, L.T.J.J.o.t.A.C.S. Thompson, High activity carbide supported catalysts for water gas shift, 133 (2011) 2378-2381.
[45] M.D. Porosoff, X. Yang, J.A. Boscoboinik, J.G.J.A.C.I.E. Chen, Molybdenum carbide as alternative catalysts to precious metals for highly selective reduction of CO2 to CO, 53 (2014) 6705-6709.
[46] J. Gao, Y. Wu, C. Jia, Z. Zhong, F. Gao, Y. Yang, B.J.C.C. Liu, Controllable synthesis of α-MoC1-x and β-Mo2C nanowires for highly selective CO2 reduction to CO, 84 (2016) 147-150.
[47] B. Yan, Y. Gao, B. Wang, X. Fan, F. Alam, J. Li, T.J.C. Jiang, Enhanced Carbon Dioxide Oxidative Dehydrogenation of 1-Butene by Iron-Doped Ordered Mesoporous Alumina, 9 (2017) 4480-4483.
[48] H. Sakurai, A. Ueda, T. Kobayashi, M.J.C.C. Haruta, Low-temperature water–gas shift reaction over gold depositedon TiO2, (1997) 271-272.
[49] A.A.f.t.A.o. Science, Small Clusters Hit the Big Time: New ways to create clusters of atoms on the nanometer scale are opening the door to quantumdot lasers, single electron transistors, and a host of other applications, American Association for the Advancement of Science, 1996.
[50] V. Colvin, M. Schlamp, A.P.J.N. Alivisatos, Light-emitting diodes made from cadmium selenide nanocrystals and a semiconducting polymer, 370 (1994) 354.
[51] Z. Liu, Z. Jian, J. Fang, X. Xu, X. Zhu, S.J.I.J.o.P. Wu, Low-temperature reverse microemulsion synthesis, characterization, and photocatalytic performance of nanocrystalline titanium dioxide, 2012 (2012).
[52] J.-l. Tang, J. Sun, Z.-G.J.C.d.t. He, Self-emulsifying drug delivery systems: strategy for improving oral delivery of poorly soluble drugs, 2 (2007) 85-93.
[53] S. Slomkowski, J.V. Alemán, R.G. Gilbert, M. Hess, K. Horie, R.G. Jones, P. Kubisa, I. Meisel, W. Mormann, S.J.P. Penczek, A. Chemistry, Terminology of polymers and polymerization processes in dispersed systems (IUPAC Recommendations 2011), 83 (2011) 2229-2259.
[54] S. Talegaonkar, A. Azeem, F.J. Ahmad, R.K. Khar, S.A. Pathan, Z.I.J.R.P.o.D.D. Khan, Formulation, Microemulsions: a novel approach to enhanced drug delivery, 2 (2008) 238-257.
[55] S.J.C.S. Moulik, Micelles: self-organized surfactant assemblies, (1996) 368-376.
[56] S.P. Moulik, B.K.J.A.i.C. Paul, I. science, Structure, dynamics and transport properties of microemulsions, 78 (1998) 99-195.
[57] J. Henle, P. Simon, A. Frenzel, S. Scholz, S.J.C.o.M. Kaskel, Nanosized BiOX (X= Cl, Br, I) particles synthesized in reverse microemulsions, 19 (2007) 366-373.
[58] J. Wang, M. Valenzuela, J. Salmones, A. Vázquez, A. Garcıa-Ruiz, X.J.C.t. Bokhimi, Comparative study of nanocrystalline zirconia prepared by precipitation and sol–gel methods, 68 (2001) 21-30.

[59] A. Monshi, M.R. Foroughi, M.R.J.W.j.o.n.s. Monshi, engineering, Modified Scherrer equation to estimate more accurately nano-crystallite size using XRD, 2 (2012) 154-160.
[60] S. Kumar, INDUCTIVE COUPLED PLASMA OPTICAL EMISSION SPECTROMETER, ANALYTICAL INSTRUMENTS, 2013.
[61] M.I. Corporation, Gemini VII Series Surface Area Analyzer Brochure, 2016.
[62] S. Afanasyev, T. Kychkina, L. Savvinova, SCANNING ELECTRON MICROSCOPE (ADVANTAGES AND DISADVANTAGES), Colloquium-journal, Голопристанський міськрайонний центр зайнятості, 2019.
[63] Transmission Electron Microscopy (TEM), 2010.
[64] Catalyst characterization - Thermal analysis.
[65] T. Instruments, Thermogravimetric Analyzers Brochure, 2018.
[66] N.W. Ockwig, T.M.J.C.r. Nenoff, Membranes for hydrogen separation, 107 (2007) 4078-4110.
[67] Y. Chen, X. Wang, X. Luo, X. Lin, Y.J.C.J.o.C. Zhang, Non-Oxidative Methane Conversion Using Lead-and Iron-Modified Albite Catalysts in Fixed-Bed Reactor, 36 (2018) 531-537.